



1 **Effect of dust on rainfall over the Red Sea coast based on WRF-Chem model simulations**

2 Sagar P. Parajuli^{*}, Georgiy L. Stenchikov¹, Alexander Ukhov¹, Suleiman Mostamandi¹, Paul A.
3 Kucera², Duncan Axisa³, William I. Gustafson Jr.⁴, and Yannian Zhu⁵

4

5

6 ¹King Abdullah University of Science and Technology, Thuwal, Saudi Arabia

7 ²National Center for Atmospheric Research, Boulder, CO 80305, USA

8 ³Center for Western Weather and Water Extremes (CW3E), Scripps Institution of Oceanography,
9 University of California, San Diego, La Jolla, California, USA

10 ⁴Pacific Northwest National Laboratory (PNNL), Richland, WA 99354, USA

11 ⁵School of Atmospheric Sciences, Nanjing University, 210023 Nanjing, China

12

13

14

15

16

17 ^{*}Corresponding Author, E-mail: sagar.parajuli@kaust.edu.sa



18 Abstract

19 Water is the single most important element of life. Rainfall plays an important role in the spatial
20 and temporal distribution of this precious natural resource and it has a direct impact on
21 agricultural production, daily life activities, and human health. One of the main elements that
22 govern rainfall formation and distribution is atmospheric aerosol, which also affects the Earth's
23 radiation balance and climate. Therefore, understanding how dust compositions and distributions
24 affects the regional rainfall pattern is of crucial, particularly in regions with high atmospheric
25 dust loads such as the Middle East. Although aerosol and rainfall research has garnered
26 increasing attention both as an independent and interdisciplinary topic in the last few decades,
27 the details of various direct and indirect pathways by which dust affects rainfall are not yet fully
28 understood. Here, we explored the effects of dust on rainfall formation and distribution as well as
29 the physical mechanisms that govern these phenomena, using high-resolution WRF-Chem
30 simulations ($\sim 1.5 \times 1.5$ km) configured with an advanced double-moment cloud microphysics
31 scheme coupled with a sectional 8-bin aerosol scheme. Our model-simulated results were
32 realistic, as evaluated from multiple perspectives including vertical profiles of aerosol
33 concentrations, aerosol size distributions, vertical profiles of air temperature, diurnal wind
34 cycles, and spatio-temporal rainfall patterns. Rainfall over the Red Sea coast is mainly caused by
35 warm rain processes, which are typically confined within a height of ~ 6 km over the Sarawat
36 mountains and exhibit a strong diurnal cycle that peaks in the evening at approximately 6 pm
37 local time under the influence of sea breezes. Numerical experiments indicated that dust could
38 both suppress or enhance rainfall. The effect of dust on rainfall were calculated as total, indirect,
39 and direct effects, based on 10-year August-average daily-accumulated rainfall over the study
40 domain covering the eastern Red Sea coast. For extreme rainfall events (domain-average daily-
41 accumulated rainfall of ≥ 1.33 mm), the total (6.05%), indirect (4.54%), and direct effects
42 (1.51%) were all positive (enhancement). At a 5% significance level, the total and indirect
43 effects were statistically significant whereas the direct effect was not. For normal rainfall events
44 (domain-average daily-accumulated rainfall < 1.33 mm), the indirect effect enhanced rainfall
45 (4.76%) whereas the direct effect suppressed rainfall (-5.78%), resulting in a negative net
46 suppressing effect (-1.02%), all of which were statistically significant. We investigated the
47 possible physical mechanisms of the effects and found that the dust direct effects were mainly
48 caused by the scattering (absorption) of solar radiation by dust. The surface cooling (warming)
49 induced by scattering (absorption) weakens (strengthens) the sea breeze circulation, which
50 decreases (increases) the associated landward moisture transport, ultimately suppressing
51 (enhancing) rainfall. Our results have broader scientific and environmental implications.
52 Specifically, although dust is considered a problem from an air quality perspective, our results
53 highlight the important role of dust on sea breeze circulation and associated rainfall over the Red
54 Sea coastal regions. Our results also have implications for cloud seeding and water resource
55 management.



56 1. Introduction

57 Rainfall rejuvenates plant and animal life. In desert regions, rain events also bring hope and
58 excitement. Rainfall affects the distribution of surface and ground water resources, which are
59 constantly declining over the Middle East and North Africa (MENA) region due to
60 overexploitation (Joodaki et al., 2014). A large proportion of global agricultural production is
61 indeed dependent on monsoon rainfall. Irregular patterns of rainfall have affected people in many
62 countries across the globe, by causing floods and droughts, affecting the regional water resources
63 (e.g., Jha et al., 2021), limiting people's access to safe drinking water, and increasing the
64 prevalence of water-borne diseases such as malaria and diarrhea (Trinh et al., 2020).

65 Dust is the dominant aerosol type in desert regions (Kalenderski and Stenchikov, 2016; Parajuli
66 et al., 2020; Ukhov et al., 2020) and it can affect regional water resources by modulating rainfall
67 distributions (Jha et al., 2021). In regions with long-term water shortages such as the Middle East
68 and North Africa (MENA), understanding the multifaceted aspects of dust-rainfall connections is
69 even more important. In desert regions, regional dust storms such as haboobs (e.g., Anisimov et
70 al., 2018) are often associated with rainfall. The older generation of people in the MENA region
71 associate certain categories of dust storms with rainfall. Due to the frequent occurrence of dust
72 storms, dust-cloud mixtures are common sights in this region.

73 Aerosol particles including dust are key to rainfall formation as they provide a surface for
74 condensation. J. Aitken, a pioneer scientist of the 18th century, said, "There would probably be
75 no rainfall if there were no dust particles in the atmosphere" (Spurny, 2000), which clearly
76 highlights the importance of dust on the Earth's climate.

77 The process of rainfall is incredibly complex and many aspects of the rain cycle remain unclear
78 despite sustained research efforts. Although the principles that govern rainfall appear highly
79 complex from a prediction perspective, the basic physics of rainfall are rather simple and
80 mesmerizing. The least understood aspects of rainfall lie within the clouds, particularly the
81 mechanisms by which aerosols affect clouds and the subsequent rainfall.

82 Given that the multiple effects of aerosols on the Earth's climate occur through various direct
83 and indirect pathways, disentangling their effect on rainfall is not easy. Furthermore, previous
84 studies on the effects of aerosols on rainfall have reported contradicting results, with some
85 indicating that dust enhances rainfall while others report a suppressing effect. Generally, aerosols
86 enhance heavy rainfall events and suppress light rainfall events (Choobari, 2018; Li et al., 2011).
87 Although multiple new mechanisms have been recently proposed to explain the underlying
88 causes of these discrepancies (e.g., Fan et al. 2018; Grabowski and Morrison, 2020; Abott and
89 Cronin, 2021), these hypotheses are still debated and at times controversial (Choobari, 2018)
90 despite extensive research on the topic. Furthermore, the effect of dust depends on the type of
91 circulation (e.g., Bangalath and Stenchikov, 2015), and therefore the present study is highly
92 significant in the coastal areas where sea and land breeze circulations are active. In this work, we
93 specifically focus on the coastal regions of the Red Sea to explore the effects of dust on rainfall.
94 We chose this region because dust-rainfall interaction should be prominent here, if any, given the
95 high levels of atmospheric dust in the region.



96 The effects of aerosol on climate are generally classified into three categories – direct, semi-
97 direct, and indirect effects (Lohmann and Feichter, 2001; Forkel et al., 2012; Zeinab et al., 2020),
98 all of which affect rainfall in unique ways. Aerosol particles directly affect radiation through
99 scattering and absorption, which is generally known as the “direct aerosol effect.” These effects
100 on radiation leads to changes in temperature, wind speed, relative humidity, and atmospheric
101 stability, all of which are collectively referred to as aerosol “semi-direct effects” (Hansen, et al.,
102 1997). Furthermore, the effects of aerosols through clouds are classified as indirect effects
103 (Twomey, 1991), which in turn are sub-classified into two types. The formation of cloud
104 condensation nuclei (CCN) or ice nuclei (IN) (Dennis, 1980; Stull, 2000) changes the cloud
105 optical properties, particularly cloud albedo, and this is referred to as the “first indirect effect”
106 (Kravitz et al., 2014). The subsequent changes in cloud cover, cloud lifetime and rainfall are
107 referred to as the “second indirect effect” (Lohmann and Feichter, 2001). In the literature, these
108 effects are commonly calculated in terms of “radiative forcing.” However, here, we calculate
109 how these effects translate into rainfall amounts, to gain insights into the effects of dust on
110 rainfall from a water resources perspective.

111 Dust can both increase and decrease rainfall by affecting local atmospheric circulation (Jacobson
112 et al., 2006; Rémy et al., 2015). For example, in West Africa, dust can reduce rainfall by
113 inducing a cooling effect that decreases the meridional gradient of moist static energy (Konare et
114 al., 2008). In contrast, dust can also enhance rainfall through dust-induced diabatic warming in
115 the upper troposphere, which enhances regional circulation (Jin et al., 2015) through the
116 “elevated heat pump” (EHP) effect (Lau et al., 2010). Dust can act both as IN (Creamean et al.,
117 2013; Jha et al., 2018), which mainly affect cold cloud processes (Ansmann et al., 2005), and
118 CCN, which primarily affect warm cloud processes (Li et al., 2010; Twohy, 2015; Jha et al.,
119 2018). Nucleation is more effective when the CCN are hydrophilic. Although dust particles are
120 weakly hydrophilic, they are larger and are activated at a higher supersaturation compared to
121 other anthropogenic aerosol species (Karydis et al., 2011).

122 Increases in aerosol concentration increase the number of cloud droplets by shifting the aerosol
123 spectrum towards smaller radii for a fixed liquid water content, which ultimately renders the
124 autoconversion or collision-coalescence process in warm clouds less efficient and increases the
125 cloud reflectivity, thus inducing a cooling effect on the Earth’s surface (Albrecht, 1989;
126 Choobari, 2018). Aerosol particles can reduce the cloud fraction by slowing down rain formation
127 by collision/coalescence (Rosenfeld et al., 2000; Jacobson et al., 2006; Min et al., 2008) but they
128 can also increase via the invigoration of convective clouds (Koren et al., 2005). Aerosol
129 invigoration is a process in which aerosols delay the rainfall in the initial stage of convection but
130 causes more rainfall in the mature stage due to the formation of deeper and larger clouds
131 (Andreae et al., 2004; Koren et al., 2005; Koren et al., 2008; Chakraborty et al., 2018; Fan et al.,
132 2018). The presence of fine aerosol particles in the atmosphere facilitates the formation of
133 smaller cloud droplets and therefore suppresses rainfall initially. This suppression allows the
134 cloud droplets to reach the freezing point as they rise to higher altitudes. Upon freezing, these
135 hydrometeors release more latent heat, which ultimately intensifies convective updrafts and
136 associated cold rainfall (Koren et al., 2008; Lee et al., 2011). One more reason for these
137 contrasting effects is that the aerosols behave differently in different cloud types. For example, a



138 dust layer below a warmer cloud base at approximately 3 km can suppress cloud formation by
139 heating, but in a higher cloud base, cloud formation can be strengthened through the contribution
140 of CCN/IN (Yin and Chen, 2007). Similarly, the effective radius of ice particles decreases with
141 increased aerosol optical depth (AOD) in high clouds, whereas it increases for low clouds (Zhao
142 et al., 2019). The rainfall response also depends on whether clouds are located over the continent
143 or the ocean (Yin et al., 2002), or whether they are located over pristine remote areas or hazy
144 urban regions (Solomos et al., 2011).

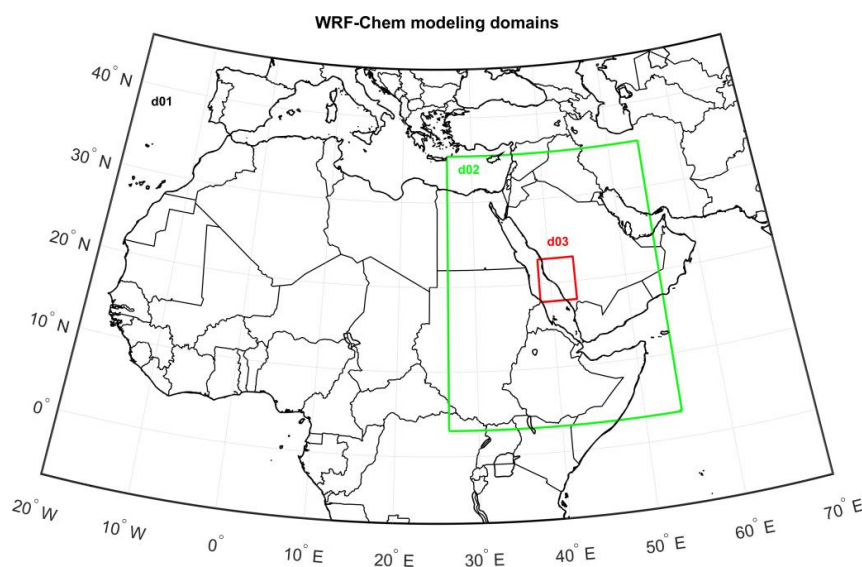
145 In summary, the effects of aerosol or dust on rainfall are governed by multiple microphysical,
146 dynamic and radiative interactions, which can either suppress, enhance, or cause no net effect on
147 rainfall depending on the regional geography (Andreae et al., 2004; Han et al., 2009). Therefore,
148 regional modeling approaches (e.g., Konare et al., 2008; Zhang et al., 2017; Jordan et al., 2020)
149 are necessary to understand the regional effects of dust on rainfall. Our study focused on the Red
150 Sea Arabian coast, which is among the regions with the highest moisture transport, and where
151 both natural (dust) and anthropogenic aerosols exist in high concentrations. Using the Weather
152 Research Forecast model coupled with Chemistry (WRF-Chem) (Grell et al., 2005) model
153 simulations supported by extensive validation of meteorology, aerosol properties, and
154 microphysical parameters, our study aimed to understand the following research questions:

- 155 1. Does dust enhance or suppress rainfall? What physical mechanisms are responsible for
156 any enhancement or suppression effect?
- 157 2. How does dust interact with local breeze circulations?

158 **2. Methods**

159 **2.1. Study domain**

160 Our study was conducted in a small domain over the Red Sea coast, as indicated by the red box
161 (d03) in Fig. 1. The study area covers the King Abdullah University of Science and Technology
162 (KAUST), Thuwal, in the north and the city of Abha in the south, the latter of which is famous
163 for its high mountains and rainfall. The domain covers a full section of the Red Sea, the Sarawat
164 Mountain range that runs from north to south, and a good portion of the nearby inland deserts
165 (d03). The study domain is encompassed by a middle domain d02, which covers a large part of
166 the Arabian Peninsula and northeast Africa, where major dust exchange occurs between the two
167 continents across the Red Sea (Kalenderski and Stenchikov, 2016). The outer domain d01, which
168 is rather large, covers the entire MENA region and includes all regional aerosol sources, as
169 described in Parajuli et al., 2020.



170

171 Figure 1. Study area over the Red Sea coast (d03). WRF-Chem model simulations were
172 conducted using the nested domains d01, d02, and d03.

173 Precipitation over the Red Sea coast is governed by the complex interactions between sea
174 breezes, local topography, and upper-level thermodynamics (Kucera et al., 2010). A moisture
175 convergence boundary is created when the moist air from the sea (driven by sea breezes) that is
176 orographically lifted along the mountain slope meets the dry Harmattan winds originating from
177 the desert, which induces convective cloud development (Kucera et al., 2010; Parajuli et al.,
178 2020).

179 Land and sea breezes (Simpson, 1994; Miller et al., 2003) are key components of the local
180 atmospheric circulation that affect the rainfall pattern over the Red Sea coast. During the
181 daytime, the coastal plains of the Red Sea become warmer, thus creating a pressure low. The
182 moisture-laden air from the Red Sea then flows towards the low-pressure region, giving rise to
183 sea breezes (Khan et al., 2015; Parajuli et al., 2020). At nighttime, the land cools down often
184 below the sea surface temperature particularly during the winter, which drives land breezes that
185 flow from the land to the sea (Parajuli et al., 2020).

186 2.2. Observations

187 Our study employed rainfall data from a recently developed algorithm called the Integrated
188 Multi-satellite Retrievals (IMERG) for Global Precipitation Measurement (GPM), which
189 combines data from the GPM constellation with the earlier precipitation estimates from TRMM
190 (Tropical Rainfall Measurement Mission) (Liu et al., 2012) to increase coverage, accuracy, and
191 resolution (Huffman, et al., 2019). We specifically used the level-3 gauge-calibrated multi-
192 satellite precipitation estimate (PrecipitationCal) V06 dataset available daily at a spatial
193 resolution of $0.1^\circ \times 0.1^\circ$.



194 Additionally, our study used Moderate Resolution Imaging Spectroradiometer (MODIS) level-2
195 Deep Blue AOD data (Hsu et al., 2004), which are available daily for the whole globe, at a
196 resolution of $\sim 0.1^\circ \times 0.1^\circ$. We also used the MODIS AOD collection 6 dataset (Hsu et al.,
197 2013), which features an improved Deep Blue aerosol retrieval algorithm. Data analyses were
198 conducted using the daily average AOD from the Terra and Aqua satellites, which encompassed
199 measurements at $\sim 10:30$ am and $\sim 1:30$ pm local time, respectively.

200 Model comparisons were conducted using the aerosol optical depth (AOD) from Aerosol
201 Robotic Network (AERONET) (Holben et al., 1998) and aerosol vertical profiles from
202 micropulse lidar (MPL) (Parajuli et al., 2020; Lopatin et al., 2021), both from the KAUST station
203 (22.3N, 39.1E). We also used cloud-screened and quality-assured level-2 AERONET AOD data,
204 which were retrieved using the direct sun algorithm. We also use AERONET V3, level-2 aerosol
205 number density and particle size distribution (PSD), which were obtained by inversion (Dubovik
206 et al., 2000) and provides volume concentrations in 22 bins between a 0.05 and 15 micron radius
207 (e.g., Parajuli et al., 2019). The LIDAR aerosol vertical profiles were retrieved using the GRASP
208 algorithm following a multi-pixel approach that allows both daytime and nighttime retrievals
209 with the use of collocated AERONET data (Dubovik et al., 2011; Parajuli et al., 2020; Lopatin et
210 al., 2020).

211 Modern-Era Retrospective Analysis for Research and Applications version 2 (MERRA-2) data
212 (Rienecker et al., 2011) were also used for model comparison.

213 Wind speed data from the KAUST station (Farrar et al., 2009) and radiosonde temperature data
214 were obtained from King Abdul Aziz International Airport, Jeddah (41024-OEJN: 21.70N,
215 39.18E) available from: <http://weather.uwyo.edu/upperair/sounding.html>.

216 CCN number concentrations were retrieved from VIIRS data following the Automated Mapping
217 of Convective Clouds (AMCC) algorithm (Yue et al., 2019) to validate our model results. The
218 algorithm extends the novel idea proposed by Rosenfeld et al. (2012) to simultaneously retrieve
219 the CCN concentrations and the cloud base updraft speeds using visible and infrared satellite
220 data. The number of activated CCN in a convective cloud base can be calculated as a function of
221 cloud drop effective radius (varies with altitude as in an adiabatic cloud), which can be retrieved
222 from a satellite imager with high-resolution wave bands such as the VIIRS (Visible Infrared
223 Imaging Radiometer Suite) onboard the Suomi NPP (National Polar-Orbiting Satellite) (Freud et
224 al., 2011; Rosenfeld et al., 2012; Rosenfeld et al., 2014). Similarly, the cloud base updraft speeds
225 can be estimated as a linear function of cloud-base height (Zheng and Rosenfeld, 2015;
226 Rosenfeld et al., 2016; Yue et al., 2019).

227 After identifying the convective cloud cells, the CCN number concentrations from the VIIRS
228 satellite were retrieved at different cloud base heights (~ 0.5 – 5.5 km) representing different
229 locations and times, which resulted in 14 days of data availability in August 2015. For
230 comparison, we first extracted the CCN concentrations for each of the 14 days of satellite
231 observations closest to the measurement time from the hourly model output. Next, the 3-d model
232 data were interpolated along the latitude, longitude, and altitude (cloud base) of the satellite data
233 points. The satellite data represented a range of supersaturations, and therefore only the data that



234 fell within the modeled supersaturation range (0.02–1.0%) were extracted for further processing.
235 The model CCN number concentrations were available at supersaturations of $S = 0.02, 0.05, 0.1,$
236 $0.2, 0.5,$ and 1.0% , therefore, for comparison, the model CCN concentrations at the points of
237 satellite-retrieved supersaturations were obtained by fitting a 3rd order polynomial on the model
238 concentrations vs. supersaturations plot at the six model points.

239 We also used CCN number concentrations measured using a Droplet Measurement Technologies
240 (DMT) CCN counter (Roberts and Nenes, 2005) during a field campaign in the Abha region of
241 Saudi Arabia in August 2009 (Kucera et al., 2010). CCN number concentrations were measured
242 at a PME (Presidency of Meteorology and Environment) ground station (18.24N, 42.46E) using
243 a CCN counter (1–10 micron) at multiple supersaturations ($S = 0.2$ and 0.7% were used for
244 comparison in this study). The model CCN number concentrations at the observation points of S
245 $= 0.2$ and 0.7% were obtained by fitting a 3rd order polynomial equation on the model
246 concentrations corresponding to the six model supersaturations, as mentioned previously.

247 Size-resolved aerosol concentrations were collected from a research aircraft (A Beechcraft King
248 Air B200) during the field campaign (August 2009) with multiple probes including a Particle
249 Measuring Systems (PMS) Forward Scatter Spectrometer Probe (FSSP-100, range 3, 0.5–8 μm
250 diameter) (Dye and Baumgardner, 1984) and a Passive Cavity Aerosol Spectrometer Probe
251 (PCASP) (0.1–3 μm diameter) (Kucera et al., 2010). For particle size comparisons, model data
252 were averaged within the range of flight times (06:00 to 10:00 UTC) during the flight days
253 (August 11–30, 2009). The model aerosol concentrations at the exact observation point along the
254 flight track with a given latitude, longitude, and altitude were determined via 3-d linear
255 interpolation of the model data.

256 **2.3. Model simulations**

257 **2.3.1. WRF-Chem model set-up**

258 High-resolution simulations are usually conducted for several days or weeks due to their high
259 computational demand. Simulating full-scale aerosol-climate interactions including indirect
260 effects adds further computational burdens. Therefore, considering our purpose, we conducted
261 our model simulations using WRF-Chem at a cloud resolving spatial resolution of 1.5×1.5 km
262 for an entire month (August), of which the first three days were discarded for spin-up. Most
263 model evaluations and diagnostic calculations were performed for a reference year (August
264 2015) unless otherwise mentioned. Additional validations are carried out for August 2009
265 because aerosol size distributions and microphysical data from a field campaign were available
266 during this period. To obtain statistically meaningful calculations of the dust effect on rainfall, 10
267 years of simulations (2006–2015) were conducted specifically for August of each year. The
268 simulations were conducted over the Red Sea coast outlined by the nested domain d03 (Fig. 1),
269 in which the parent domains d02 (4.5×4.5 km) and d01 (13.5×13.5 km) cover the Arabian
270 Peninsula/northeast Africa and the MENA region, respectively. August was chosen because
271 during this month the Red Sea coast receives abundant rainfall and sea breezes are relatively
272 strong, which plays an important role in moisture transport over the coastal plains (Mostamandi
273 et al., 2021).



274 The initial and lateral boundary conditions were obtained using European Centre for Medium-
275 Range Weather Forecasts (ECMWF) operational analysis 6-hourly data downloaded at F640
276 Gaussian grids (~15 km). The sea surface temperature (SST) was also updated every 6 hours
277 using the skin temperature field from the same ECMWF dataset.

278 To better represent cloud processes, it is important to use well-developed aerosol chemistry and
279 microphysical schemes (Zhang et al., 2016). Here, we adopted the Model for Simulating Aerosol
280 Interactions and Chemistry (MOSAIC) scheme (Fast et al., 2006; Zaveri et al., 2008; Zhao et al.,
281 2011) with eight sectional aerosol bins. The MOSAIC scheme is computationally intensive and
282 generates large outputs, as all aerosol concentrations are reported for the eight MOSAIC bins for
283 interstitial and in-cloud aerosols. Our simulations used chem_opt = 10, which couples the CBMZ
284 (carbon bond mechanism) gas phase chemical mechanism (Zaveri and Peters, 1999) with the
285 MOSAIC aerosol scheme, and is one of the most developed chemical mechanisms within WRF-
286 Chem.

287 MOSAIC includes both interstitial and cloud-borne aerosols, cloud-aerosol interactions,
288 activation/resuspension, nucleation, coagulation, aqueous chemistry, and wet removal (Fast et
289 al., 2006; Gustafson et al., 2007). Here, we particularly focused on accurately representing dust
290 aerosols because it is a specific driving force in the region. MOSAIC includes all aerosols of
291 interest including dust (included in other inorganic aerosols or “oin” because it is chemically
292 inert), sea salt, sulfate, BC, and OC (Zhao et al., 2011; Zaveri et al., 2008). Within our model
293 setup, aerosols affect clouds and clouds also affect aerosols, e.g., through in-cloud scavenging
294 and by forming sulfate aerosols (Yang et al., 2012). Aerosol particles are assumed to be
295 internally mixed and Köhler’s theory is used to relate the aerosol size distribution and
296 composition to the activated CCN as a function of the maximum supersaturation (Abdul-Razzak
297 and Ghan, 2002; Yang et al., 2012). Aerosol activation from the interstitial to in-cloud state is
298 calculated based on a maximum supersaturation determined from a Gaussian spectrum of updraft
299 velocities and internally mixed aerosol properties within each size bin (Chapman et al., 2009).
300 When the hydrometeors evaporate, particles return to the original interstitial phase (Yang et al.,
301 2012).

302 In MOSAIC, dust is treated as part of the internal mixture used across all aerosol species. Dust
303 emissions contribute dust mass to the different size bins as ‘oin’ (other inorganics). All gas and
304 aerosol processes (e.g., sulfate formation) operate within the mixture but dust itself does not take
305 part in the chemical reactions, although MOSAIC includes the chemical reaction of CaCO₃ (a
306 constituent of dust) with acids when the proportion of CaCO₃ is provided (Zaveri et al., 2008).
307 Dust itself is considered weakly hydrophilic in WRF-Chem with a hygroscopicity of 0.14
308 (Kawecki and Steiner, 2018). However, chemical processes within the aerosol mixture may
309 affect the activation of CCN/IN, which ultimately affects precipitation (Abdelkader et al., 2017;
310 Klingmüller et al., 2019). This is because interstitial aerosols are partially activated as CCN (in-
311 cloud or cloud-borne aerosols) at each grid cell and time step by using a volume-weighted bulk
312 hygroscopicity from all aerosol species (e.g., dust, sulfate, oin, sea salt) within each size bin
313 (Kawecki and Steiner, 2009; Tuccella et al., 2015) as a function of the environmental
314 supersaturation (Abdul-Razzak & Ghan, 2000). Reduction due to chemical and physical (e.g.,



315 coagulation) processes, as well as particle growth, will also cause particles to shift across
316 different bins (Abdul-Razzak and Ghan, 2002; Chapman et al., 2009). The volume-average
317 refractive index within a given size bin is used to calculate the optical properties using Mie
318 theory (Tuccella et al., 2015). Therefore, dust can affect both direct and indirect aerosol
319 feedback.

320 For cloud microphysics, we used the Morrison double-moment scheme (Morrison et al., 2009),
321 which is one of the commonly used microphysics options in WRF. This scheme allows for the
322 prognostic treatment of two moments of the hydrometeors (mixing ratios and number
323 concentrations) for five species (cloud droplets, cloud ice, snow, rain, and graupel), while
324 calculating key microphysical processes such as autoconversion, collection between hydrometeor
325 species, melting/freezing, and mass transfer from snow to ice (Yang et al., 2011). Compared to
326 the single-moment scheme, which only predicts mixing ratios, the double-moment approach can
327 better represent precipitating convective clouds particularly during heavy precipitation episodes
328 (Lim et al., 2010). The size distribution of hydrometeors is prescribed from the predicted bulk
329 number and mass mixing ratios of different hydrometeor types in an assumed gamma size
330 distribution (Gao et al., 2016). The prognostic treatment of the CCN distribution improves the
331 simulated cloud properties and radiative effects compared to a prescribed uniform CCN
332 distribution, albeit at an increased computational cost (Gustafson et al., 2007). The physics and
333 chemistry namelist options used in our WRF-Chem set up is summarized in Table 1.

334

335 Table 1. Physics and chemistry namelist settings used in WRF-Chem.

Description		Namelist Options	References
Physics	Microphysics	mp_physics = 10	Morrison double-moment scheme (Morrison et al., 2009)
	Planetary Boundary Layer (PBL) scheme	bl_pbl_physics = 1	Yonsei University Scheme (YSU) (Hong, et al., 2006)
	Surface layer physics	sf_sfclay_physics = 1	Revised MM5 Monin-Obukhov scheme (Jimenez, renamed in v3.6)
	Land Surface Model	sf_surface_physics = 2	Unified Noah land surface model (Tewari et al., 2004)
	Cumulus parameterization	cu_physics = 0 (turned off)	
	Radiative transfer model	ra_lw_physics = 4, ra_sw_physics = 4	Rapid Radiative Transfer Model (RRTMG) for both shortwave and longwave (Iacono et al., 2008)
Chemistry	Chemistry option	chem_opt = 10 (8)	CBMZ chemical mechanism with MOSAIC 8-bin sectional aerosol scheme (MOSAIC 8-bin aerosol scheme)
	Dust scheme	dust_opt = 13	GOCART dust emission scheme coupled with MOSAIC aerosol scheme
	Photolysis scheme	phot_opt = 1	Madronich photolysis (TUV)



336 We included sea salt emissions using a parameterization based on 10-m wind speed (Monahan et
337 al. 1986; Gong, 2003). Anthropogenic aerosol emissions were also included in our simulations.
338 The emission of sulfur dioxide (SO₂), which chemically transforms to sulfate aerosols, is
339 prescribed using OMI (ozone monitoring instrument)-HTAP (Task Force Hemispheric Transport
340 Air Pollution) data for 2015 developed by the National Aeronautics and Space Administration
341 (NASA), as in Parajuli et al., 2020. Other emissions including BC and OC as well as SO₂ ship
342 emissions are prescribed using the EDGAR (Emission Database for Global Atmospheric
343 Research) database v4.3.2 available at a 0.1° × 0.1° resolution (Crippa et al., 2018).

344 The cloud-aerosol interactions on shortwave (SW) radiation are represented by linking the cloud
345 droplet number concentration predicted by the microphysics scheme with the RRTMG
346 shortwave radiative scheme. Aerosol direct radiative effects through longwave (LW) are also
347 calculated using the RRTMG scheme (Iacono et al., 2000; Zhao et al., 2011). Aerosol indirect
348 effects are calculated following Gustafson et al. (2004) to include both first and second indirect
349 effects. Aerosol particles acting as CCN are coupled with the Morrison microphysics scheme,
350 which allows aerosols to affect the cloud droplet number and cloud radiative properties, while
351 also allowing clouds to alter aerosol size and composition through aqueous processes and wet
352 scavenging (Gustafson et al., 2004). We explicitly resolved the updrafts using a cloud-resolving
353 spatial resolution in the inner domain (d03).

354 In MOSAIC, aerosol emissions are independently calculated within its own module in which the
355 dust emission is calculated using the original GOCART dust scheme (Ginoux et al., 2001) as
356 described by Zhao et al. (2010), which is called by setting dust_opt = 13. Note that this option
357 was not implemented in the version of WRF-Chem used herein (3.8.1), but we ported this change
358 into our setup (within the subroutine module_mosaic_addemiss.F). We also accounted for
359 gravitational settling of aerosols in this work similar to Ukhov et al. (2021), which has not been
360 implemented for the MOSAIC scheme in WRF-Chem.

361 To represent dust sources, we used the topographic source function developed by Ginoux et al.
362 (2001), which is calibrated to match the simulated AOD with observed AOD as in Parajuli et al.
363 (2020). To accurately simulate the effect of dust on cloud formation and rainfall, it is important
364 to ensure that the simulated AOD is consistent with the observations. The AOD is highly
365 sensitive to the size distribution of the dust particles (Ukhov et al., 2021). Therefore, we
366 iteratively adjusted the emission size distribution to match the volume size distribution of
367 aerosols obtained from AERONET as described by Ukhov et al. (2020). There are two places in
368 which the dust size distributions can be adjusted within WRF-Chem. First is the size distribution
369 of the “emitted dust” prescribed in five bins within the GOCART dust scheme, which is
370 specified in phys/module_data_gocart_dust.F. The second is the dust size fractions used by the
371 MOSAIC aerosol scheme (8 bins) specified in chem/module_mosaic_addemiss.F. Both of these
372 size fractions were modified to obtain a closer fit to the AERONET volume size distributions.
373 The modified and the default size fractions are presented in Table S1 and S2.



374 2.3.2. Experiments

375 Designing an appropriate experiment to determine the effect of dust in a model is challenging.
 376 For example, one can consider a ‘baseline’ simulation with ‘clear’ conditions without any
 377 aerosols and then add dust to see how it affects the rainfall. However, ‘clear’ conditions are
 378 hardly ever observed and thus it is unrealistic to design an experiment with zero rainfall.
 379 Therefore, we first considered a real-world scenario as a baseline by including all aerosols (dust,
 380 sea salt, sulfate, organic, and black carbon) similar to Klingmüller et al. (2019), in which the
 381 resulting rainfall closely matches the observed rainfall pattern (Table 2, F1). The baseline
 382 experiment is calibrated against MODIS/AERONET AOD data as mentioned previously and
 383 thus exhibited a realistic aerosol distribution in terms of optical depth, PSD, and vertical profiles,
 384 as well as the rainfall pattern (see section 3.2.1). The second experiment is the ‘no_dust’
 385 experiment (Table 2, F2) in which we assigned ‘zero’ values to the source function in the dust
 386 emission equation (Parajuli et al., 2019), thereby effectively eliminating dust emissions from all
 387 grid cells in all three domains. Both of the aforementioned experiments include aerosol-radiation,
 388 aerosol-cloud, and microphysical interactions, and therefore they represent the total effect (both
 389 direct and indirect) of aerosols. From a practical perspective, the all_aer experiment represents a
 390 ‘real world’ scenario in which all aerosols including dust are included to obtain a realistic rainfall
 391 pattern, whereas the no_dust experiment represents rainfall in an idealized, dust-free world. We
 392 also conducted two additional experiments (F3 and F4) to separate the aerosol direct effects from
 393 indirect effects. In these two simulations, we restricted aerosol-radiation interactions
 394 (aer_rad_feedback = 0), both in all_aer (F3) and no_dust (F4) cases, while keeping all the model
 395 physics and domain settings the same as in the previous two experiments. Therefore, these latter
 396 two experiments essentially represent the indirect effects only.

397 The total effect (Δ_{Tot}), indirect effect (Δ_{Indir}), and direct effect (Δ_{dir}) of dust were then calculated
 398 with the following equations:

$$399 \Delta_{tot} = F1 - F2 \quad (1)$$

$$400 \Delta_{indir} = F3 - F4 \quad (2)$$

$$401 \Delta_{dir} = \Delta_{Tot} - \Delta_{Indir} = (F1 - F2) - (F3 - F4) \quad (3)$$

402 Table 2. WRF-Chem model experiments

Aerosol species	Experiments with both direct and indirect effects		Experiments with indirect effects only		Experiments with direct effects only ^a		Experiments with direct effects only but without shortwave dust absorption ^b	
	F1 all_aer	F2 no_dust	F3 all_aer, no_direct	F4 no_dust, no_direct	F5 all_aer, no_indirect	F6 no_dust, no_indirect	F7 all_aer, no_indirect, no_absorb	F8 no_dust, no_indirect, no_absorb
Dust	yes	no	yes	no	yes	no	yes	no
Sea salt	yes	yes	yes	yes	yes	yes	yes	yes
Anthropogenic (sulfate, OC, and BC)	yes	Yes	yes	Yes	yes	Yes	yes	Yes

403 ^{a, b} diagnostic experiments (see section 3.3.2).



404 The physical processes through which dust affects breezes are difficult to understand when both
405 direct and indirect effects are active. Additionally, the indirect effects are more complex and
406 their representation in the model is accompanied by a high degree of uncertainty. To better
407 understand the effect of dust on breezes, we analyzed the direct effects of dust alone from an
408 independent pair of simulations involving the dust direct effects only (F5, F6, Table 2) [i.e.,
409 without considering the indirect effects (chem_opt = 8)].

410 The dust direct effect is caused by both scattering and absorption of radiation in the SW bands.
411 Therefore, to further understand the relative importance of shortwave cooling and warming
412 resulting from direct effects, we conducted an additional pair of simulations (F7, F8, Table 2), in
413 which we restricted the shortwave absorption of radiation by dust in the previous experiments F5
414 and F6. To achieve this, we changed the imaginary part of the refractive index for dust from the
415 default value of 0.003 to 0.

416 The aforementioned effects were calculated for the domain-average daily-accumulated rainfall
417 over the study period of August 4-31 for each year between 2006–2015 as the difference of
418 rainfall amounts between the experiments all_aer (x) and no_dust (y). The statistical significance
419 of the effect was determined from the entire 10 years of simulations by creating a uniform
420 sample of domain-average daily-accumulated rainfall data consisting of 280 (10×28 days) data
421 points. Statistical analysis were then conducted by separating the data into two categories:
422 extreme and normal rainfall events. This separation is meaningful because extreme rainfall
423 events are more influenced by synoptic features whereas normal rainfall events are more
424 influenced by diurnal-scale sea breeze circulation. High and low rainfall regimes are also known
425 to respond differently to a given aerosol loading (Li et al., 2011; Choobari, 2018). Extreme
426 rainfall events were separated from normal rainfall events using the 90th percentile value of the
427 rainfall data from F1 experiment, which was 1.33 mm. Specifically, days with domain-average
428 daily-accumulated rainfall values greater than or equal to 1.33 mm were considered extreme
429 rainfall events, whereas those with values below 1.33 mm were considered as normal rainfall
430 events. With this criterion, the effective numbers of samples (days) available for statistical
431 analysis were 31 and 243 for extreme and normal rainfall events, respectively. Using MATLAB,
432 the statistical significance of the effects was determined with the Wilcoxon signed-rank test
433 (Hollander and Wolfe, 1999; Gibbons and Chakraborti, 2011), which is recommended for data
434 with non-normal distributions such as rainfall. The null hypothesis of the test considered that the
435 difference [all_aer (x) – no_dust (y)] comes from a distribution with zero median. The same
436 method was applied to identify significant effects among other parameters including 2-m air
437 temperature, 10-m winds, and 2-m water vapor mixing ratio.

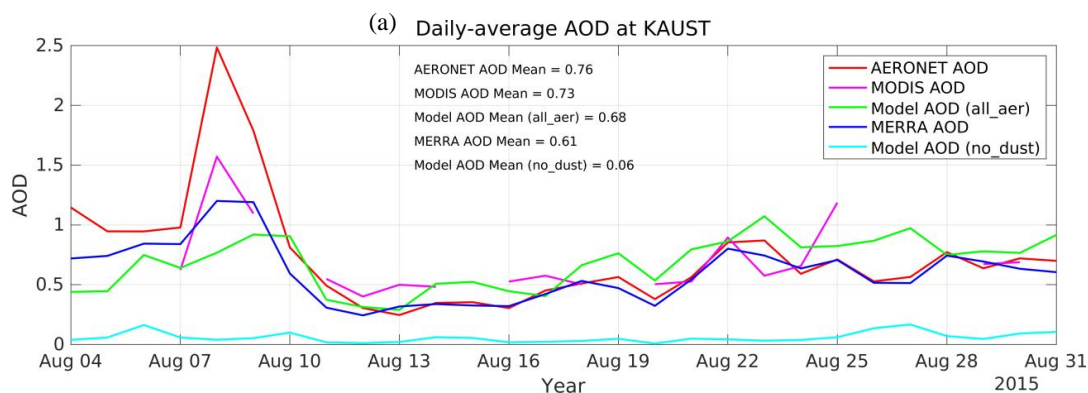
438 **3. Results**

439 **3.1. Model validation**

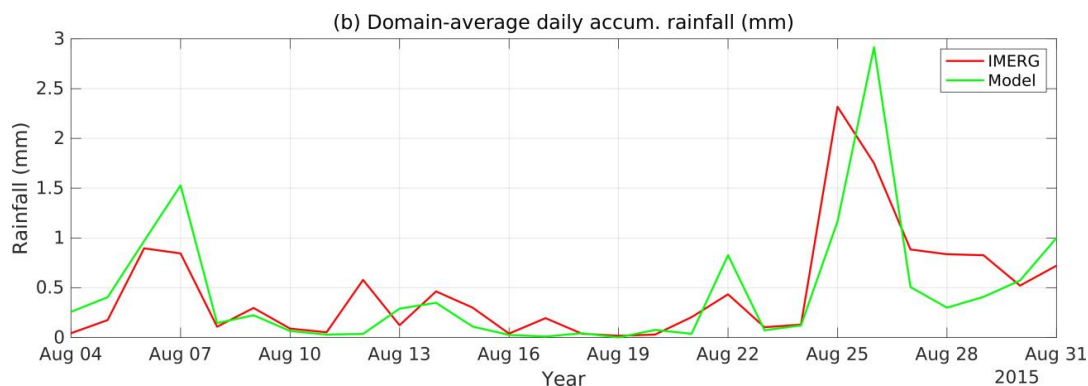
440 Here we present a comprehensive evaluation of WRF-Chem from multiple perspectives,
441 including diurnal cycles, vertical profiles, spatial distribution, and column-averaged properties,
442 before using the model for answering our research questions listed in section one. All results in
443 this section correspond to the ‘real world’ case (all_aer) unless otherwise stated.



444



445



446

447 Figure 2. (a) Simulated daily-mean total AOD as compared to MODIS and MERRA-2 data at
448 KAUST and (b) simulated daily-accumulated rainfall (mm) as compared to IMERG data,
449 averaged over the study domain (d03).

450 Figure 2a shows the domain-averaged (d03) time series of model-simulated AOD (all_aer case)
451 during the study period compared to AERONET, MODIS, and MERRA data. The model AOD
452 generally agrees well with both datasets although the peaks during the dust storm (August 8–9)
453 tend to be underestimated. The average AOD corresponding to the no_dust case is also presented
454 in Fig. 2a to provide a sense of how much AOD is increased with the addition of dust.

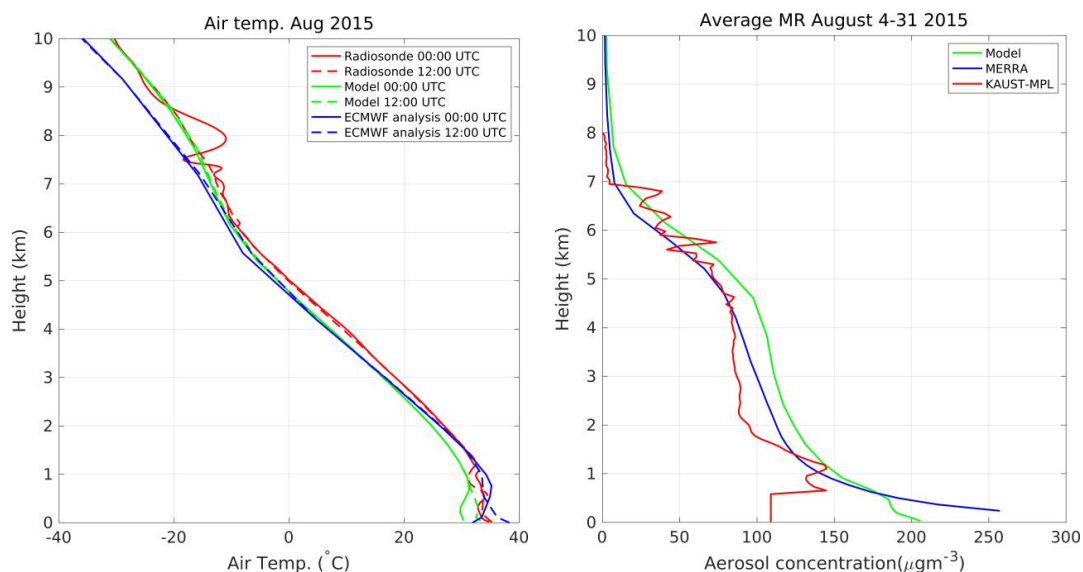
455 The time-series profile of the model-simulated daily-accumulated rainfall follows the trend in the
456 IMERG data (Fig. 2b). The rainfall peaks including the largest rain event during the study period
457 (~ Aug 25, 2015) were reproduced reasonably well. Some discrepancy is expected because there
458 are usually fewer microwave imager observations included in the IMERG data in the
459 tropical/subtropical region.

460 Fig. S1 illustrates comparison between the simulated aerosol volume size distribution and the
461 corresponding AERONET size distribution. The two distributions agreed well, especially in the
462 finer mode that is centered at ~ 0.1 microns, which is critical from the perspective of the
463 contribution of aerosols in the formation of CCN/IN. It is also important to note that this finer
464 mode was non-existent in the model when using the default aerosol size distribution. Therefore,



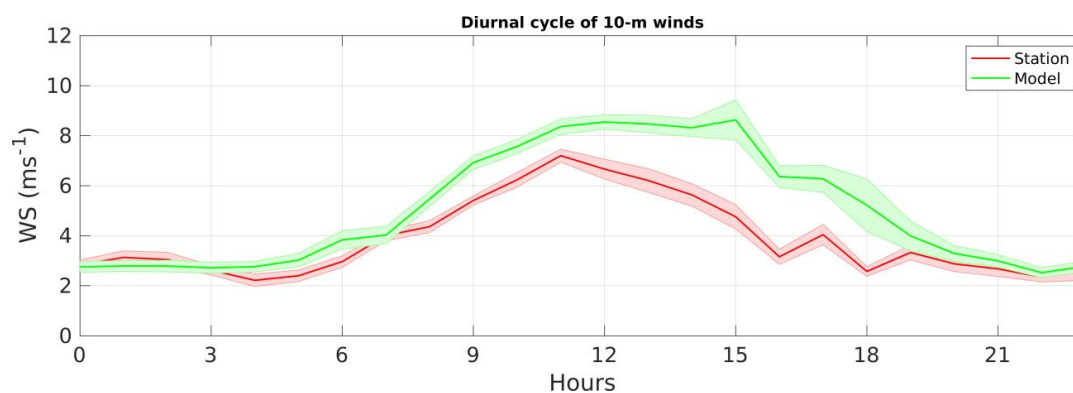
465 we adjusted both dust emission fractions (Table S1) as well as MOSAIC dust size fractions
466 (Table S2) so that the resulting size distribution matched the AERONET data more accurately, as
467 mentioned earlier.

468 Figure 3 shows the model-simulated vertical profiles of air temperature (left) and aerosol
469 concentrations (right) compared to key observations. The simulated temperature profile was
470 generally consistent with the radiosonde observations as well as ECMWF operational analysis
471 with some discrepancies at the cloud-level heights and near the surface. The temperature at the
472 site does not show large daytime and nighttime variations. Figure 3 also shows the profiles of
473 aerosol concentrations at KAUST averaged over the study period. The profiles of the model,
474 MERRA-2, and LIDAR data were identical. However, the model and MERRA-2 slightly
475 overestimated aerosol concentrations near the surface compared to the LIDAR data.



476

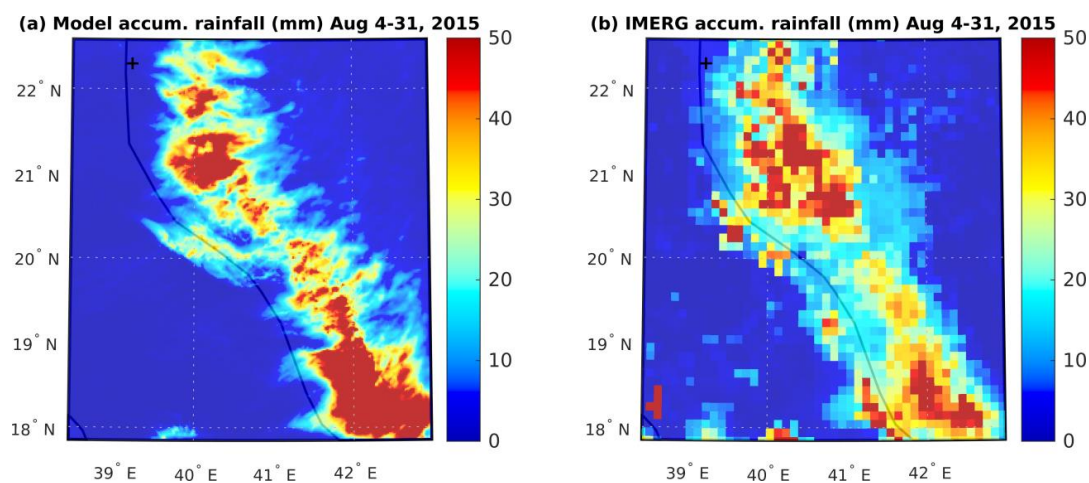
477 Figure 3. Average vertical profiles of air temperature (left) and aerosol concentrations (right)
478 compared to reference observations. The air temperature profile was compared against ECMWF
479 operational analysis and radiosonde station data at King Abdul Aziz International Airport,
480 Jeddah (21.7N, 39.18E) during the daytime (12:00 UTC) and nighttime (00:00 UTC) by
481 averaging during the study period (4–31 August 2015). Simulated aerosol mixing ratios were
482 compared against MERRA-2 reanalysis and MPL LIDAR station data at KAUST (22.30N,
483 39.10E) for 4–31 Aug 2015.



484

485 Figure 4. Diurnal profile of the model-simulated wind speeds compared to station data over the
486 study period (Aug 4–31, 2015) at KAUST (22.30N, 39.10E). The shading represents the standard
487 error of the mean calculated from the hourly wind speeds.

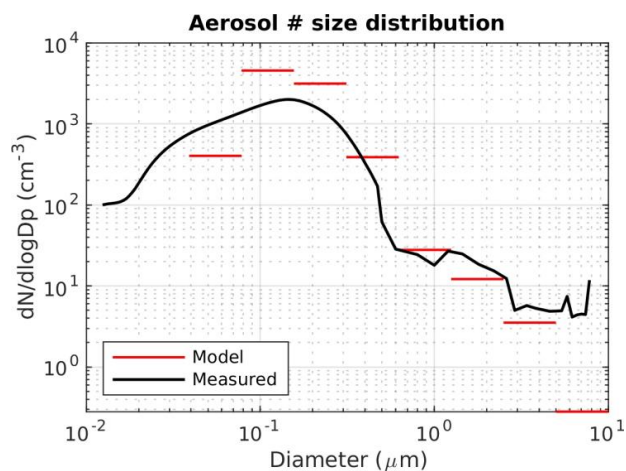
488 Figure 4 shows the wind speed diurnal profile in the model and the observations at KAUST,
489 which were reasonably consistent. The model overestimated wind speeds mainly during the
490 afternoon, which is when the flow is more chaotic as the sea breezes meet the northeasterly
491 harmattan winds. The peak winds occur at ~ 12:00 UTC (15:00 local time), which correspond to
492 the sea breeze maxima.



493

494 Figure 5. Spatial distribution of accumulated rainfall (Aug 4–31, 2015) (a) model (b) IMERG
495 data. The location of KAUST is marked by a plus sign.

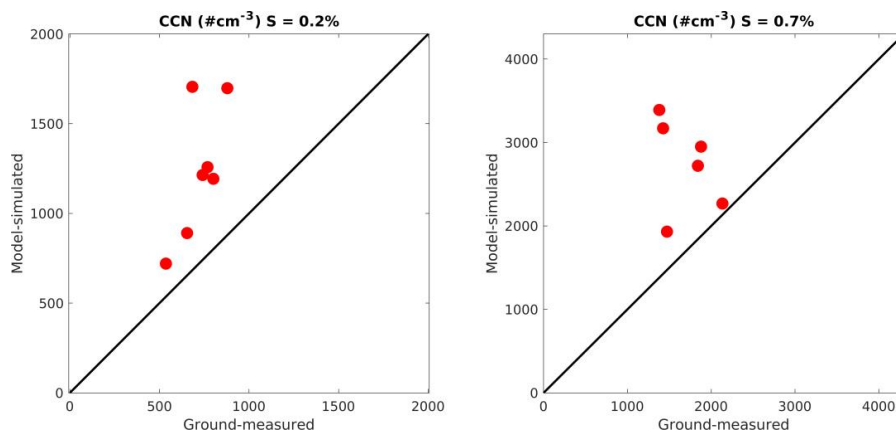
496 Figure 5 shows the spatial distribution of accumulated rainfall during the study period over the
497 study domain (d03) compared to the IMERG data, both of which were reasonably consistent
498 with each other. The rainfall pattern follows the length of the Sarawat Mountains stretching north
499 to south. The southern areas of the domain receive more rainfall due to the presence of higher
500 mountains.



501

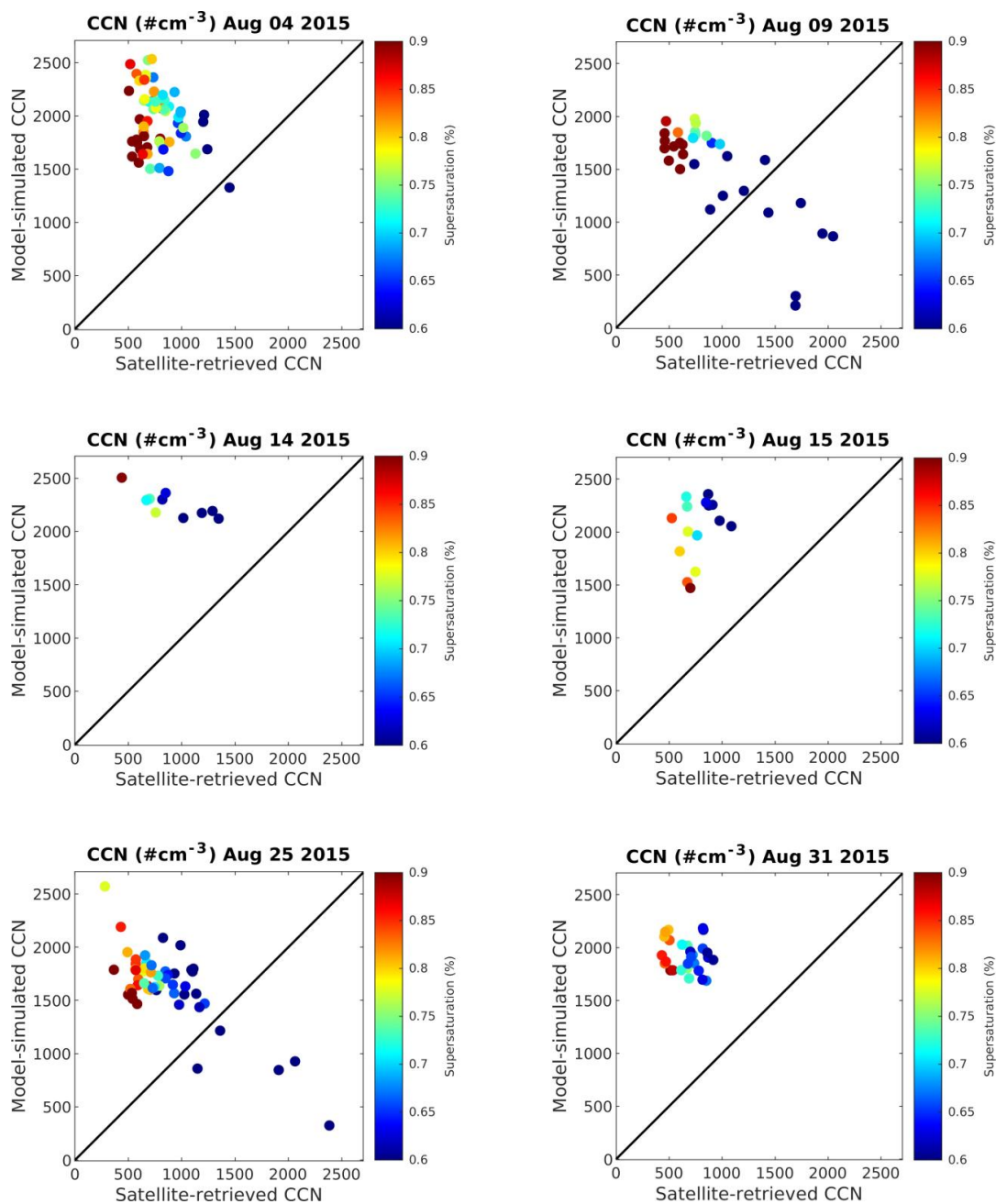
502 Figure 6. Comparison of model-simulated aerosol number concentrations (cm^{-3}) corresponding
503 to MOSAIC size bins compared to flight measured values during the field campaign of August
504 2009. The widths of the red lines represent the widths of the eight MOSAIC bins.

505 Figure 6 shows the aerosol number size distributions compared to the flight data, which were
506 reasonably similar. The model data (8-bins) were extracted at the exact latitude, longitude, and
507 altitude corresponding to the flight data by 3d linear interpolation and averaged over the days
508 available (Aug 11–30, 2009) during the time of measurements (~06:00 to 09:00 UTC).



509

510 Figure 7. Comparison between model-simulated CCN number concentrations and ground-
511 measured values at the PME station (18.24N, 42.46E) at supersaturations of 0.2 and 0.7%. The
512 CCN number concentrations correspond to the ground station at Abha. The plotted point
513 represents the average value for different days of measurement from August 11–30, 2009
514 approximately from 02:00 to 08:00 UTC.



515

516 Figure 8. Model-simulated vs. VIIRS satellite-retrieved CCN number concentrations for six days
517 of available data within the study domain during the August 2015 study period.



518 Figure 7 shows the comparison between the CCN number concentrations obtained from the
519 model and from ground station at two super-saturations measured during the Aug 2009 field
520 campaign. CCN number concentrations are generally overestimated by the model at both
521 low/high super-saturations by up to a factor of two.

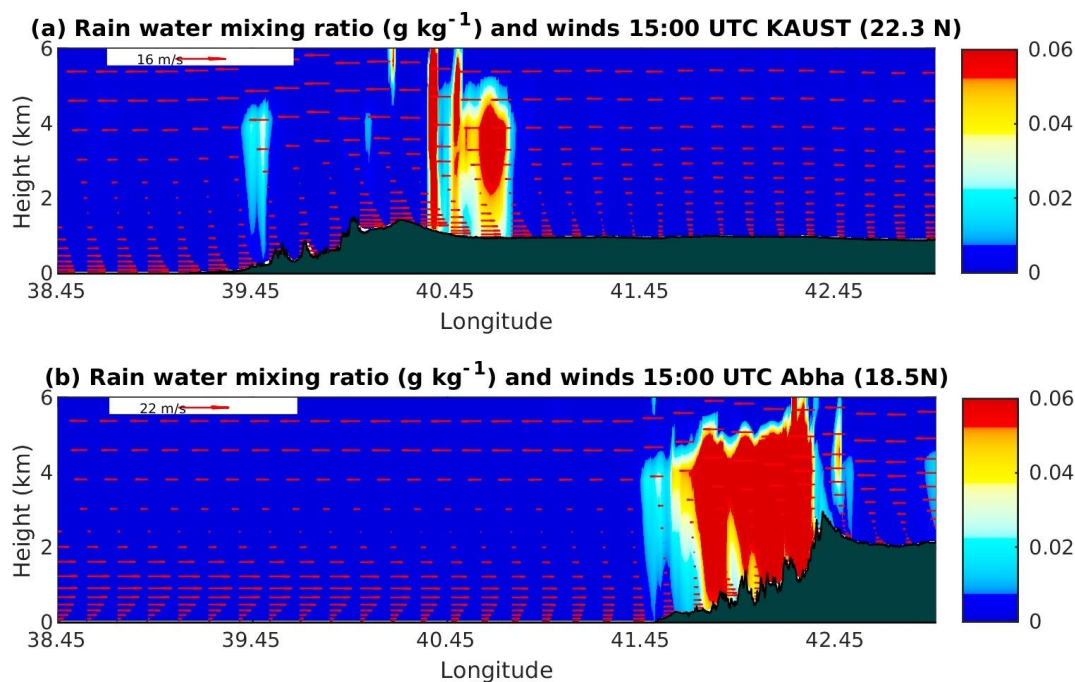
522 Figure 8 shows the comparison between the model-simulated CCN number concentration and the
523 satellite-retrieved data from VIIRS. The data points represent CCN number concentrations at the
524 cloud base of existing convective cells on different days over the study domain (d03). Similar to
525 the previous comparison, the model overestimates CCN number concentration compared to the
526 VIIRS data also by approximately a factor of two. This order of difference, although large, is
527 reasonable for microphysical parameters given the high uncertainty in their parameterization.

528 Since the rainfall amount is reasonably well simulated (Figs 2b and 5), the overestimation of
529 CCN concentration suggests that CCN is not a limiting factor for rain formation in the study
530 region. These findings are reasonable because the study region is not aerosol-limited, and
531 therefore cloud growth and rainfall do not strongly depend on the changes in CCN
532 concentrations, unlike in other aerosol-limited areas (Koren et al., 2014).

533 **3.2. Rainfall diagnostics**

534 This section presents the diagnostic results of the key parameters related to the rainfall process to
535 demonstrate the accuracy of our rainfall calculations.

536 Figures 9a and 9b show the rainwater mixing ratio in two longitudinal cross-sections, one
537 passing through KAUST (22.3N, 39.10E), a relatively dry area, and another through Abha
538 (18.25N, 42.51E), a region known for rainfall abundance. Maximum rainfall occurs in the
539 evening at 15:00 UTC (6 pm local time) at both locations in the convergence boundary (i.e.,
540 where the sea breezes meet with Harmattan winds). The rainfall is limited to a ~6 km height
541 around the hilly terrain. There is less rainfall near the coast, where the majority of the population
542 resides, because the rain evaporates well before it reaches the ground due to high surface
543 temperature. The moisture-laden sea breezes can be prominently seen during the day within ~1.5
544 km height. Furthermore, these sea breezes strengthen as they travel upslope over the Sarawat
545 Mountains (black shades). The dry northeasterly Harmattan winds, which usually bring dust
546 from the desert towards the Red Sea during dust storms (Prakash et al., 2014; Parajuli et al.,
547 2020) can be seen at a ~3–6 km height.



548

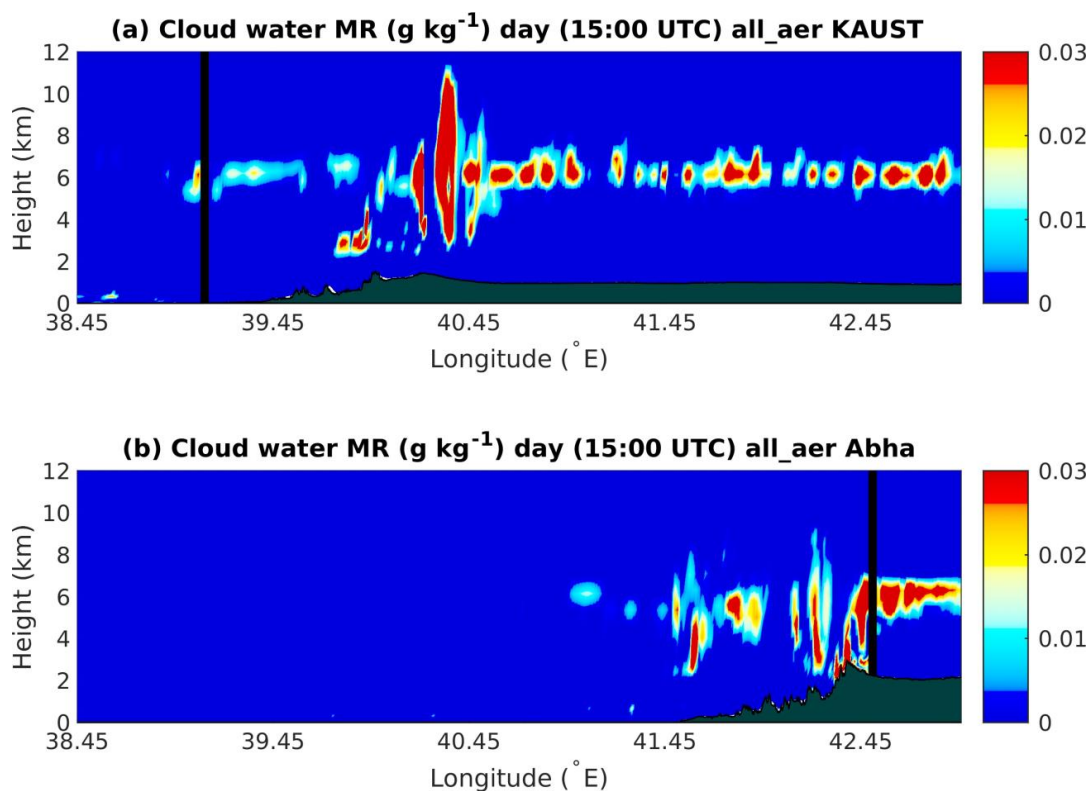
549

550 Figure 9. Rainwater mixing ratio and wind vectors averaged at the time of rainfall maxima over
551 the study period (August 4–31, 2015) at two longitudinal cross-sections passing through (a)
552 KAUST and (b) Abha.

553 Figure 10 shows the cloud water mixing ratio profiles at the longitudinal profiles passing through
554 KAUST and Abha at 15:00 UTC, which provides insights into the vertical position and extents
555 of the clouds. The locations of clouds are consistent with the locations of rainfall maxima in Fig.
556 9. Most clouds are observed at a ~5–6 km height at both locations, suggesting that the warm
557 cloud processes are responsible for causing rainfall in the region. The height of deeper,
558 convective clouds ranges from ~3 to 10 km. The clouds are generally deeper where rainfall is
559 more intense, which suggests the existence of local convective activity.

560 Although more clouds are observed over KAUST (Fig. 10a) than over the Abha region (Fig.
561 10b), more rainfall occurs over Abha because the steeper topographic slope over the Abha region
562 facilitates stronger orographic lifting of the moist air mass, which converts more easily into rain.
563 As a result, the maximum rainfall over the Abha region occurs on the front side of the mountains
564 (Fig. 9a), whereas the maximum rainfall over the KAUST region was observed on the lee side
565 (Fig. 9b). Additionally, there is more evaporation over the KAUST region due to its higher
566 surface temperature compared to the Abha region, which reduces the amount of rainfall that
567 reaches the ground but contributes to more cloud formation.

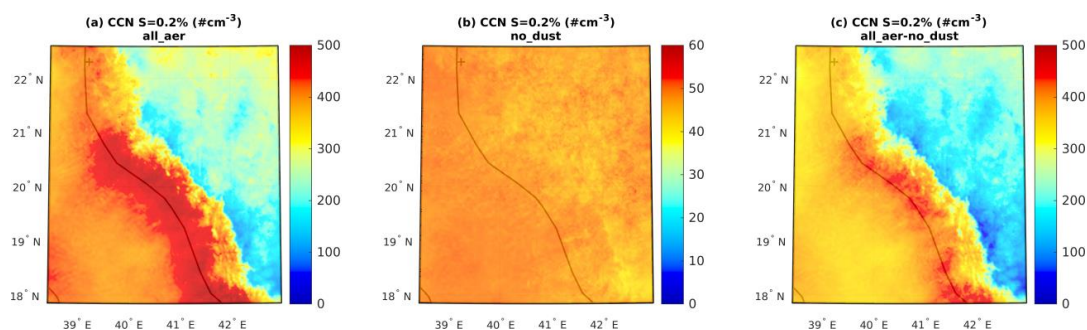
568



569

570 Figure 10. Profile of cloud water mixing ratio for a longitudinal section passing through (a)
571 KAUST and (b) Abha, averaged for August 4–31, 2015 at 15:00 UTC. The location of KAUST
572 and Abha City are indicated with black vertical lines.

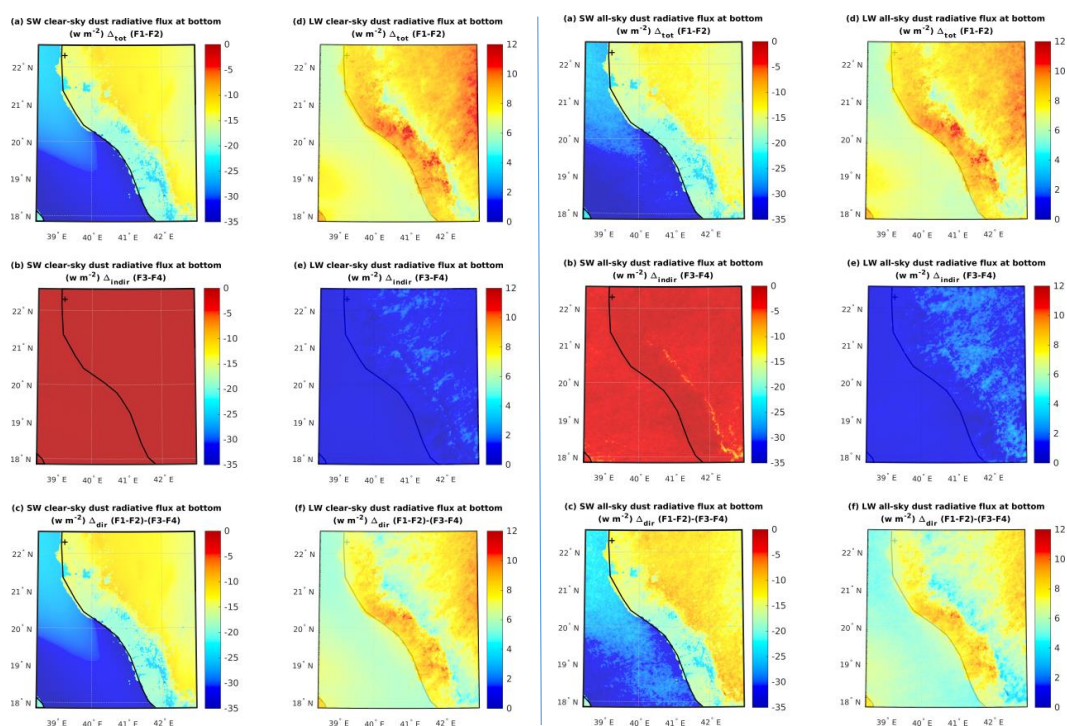
573 Figure 11 shows the spatial distribution of the CCN number concentrations at a 0.2%
574 supersaturation for all_aer (F1), nodust (F2) and their difference (F1-F2). In the absence of dust,
575 CCN # concentrations are generally uniform throughout the domain (Fig. 11b). There is up to
576 ten-fold increase of CCN after addition of dust (Fig. 11a), making dust the major contributor of
577 total CCN. The simulated CCN # concentrations in no_dust case are in the range of ~40–50 (Fig.
578 11b), which are too low compared to the observed CCN # concentrations, which are roughly in
579 the range of 500–1000 in observations (Figs. 7 and 8). Although model CCN # concentrations
580 are overestimated compared to observations as discussed previously, it is clear that addition of
581 dust brings the CCN # concentrations much closer to observations (Fig. 11a) compared to the
582 case without dust (Fig. 11b).



583

584 Figure 11. CCN number concentrations at 0.2% supersaturation at a cloud-level height (570 hPa)
 585 averaged at 15:00 UTC for August 4–31, 2015 (a) all_aer (F1), no_dust (F2), and (c) the
 586 difference F1-F2.

587



588

589 Figure 12. Effects of dust on the clear-sky (left two columns) and all-sky (right two columns)
 590 radiative fluxes at the bottom of the atmosphere calculated from 10-year August average WRF-
 591 Chem simulations.

592 To accurately evaluate the effect of dust on rainfall, it is important to ensure that the dust effects
 593 on radiative fluxes are reasonably well simulated. To gain insights into the relative importance of



594 dust and clouds on radiative budget, the effects of dust on radiative fluxes for clear-sky (without
595 clouds) and all-sky (with clouds) conditions were evaluated separately.

596 Figure 12 (left two columns) shows the effect of dust on clear-sky radiative flux in terms of total,
597 indirect, and direct effects at the bottom of the atmosphere. Dust decreases the radiative flux that
598 reaches the surface due to SW scattering and absorption, and therefore the direct effect is
599 negative, which in turn governs the total effect. The effect of dust on LW radiative flux is
600 positive because dust absorbs LW radiation. The clear-sky indirect effects are non-zero but very
601 small compared to the direct effects. These small indirect effects arise due to feedback processes
602 that cause small perturbations in cloud properties. Figure 12 (right two columns) shows the
603 effects of dust on all-sky (i.e., with clouds) radiative flux. The all-sky radiative fluxes exhibited
604 small changes in the indirect and direct effects due to the clouds both in the SW and LW bands.
605 The magnitude and sign of SW and LW dust radiative forcing are consistent with the results of
606 Klingmüller et al., 2019.

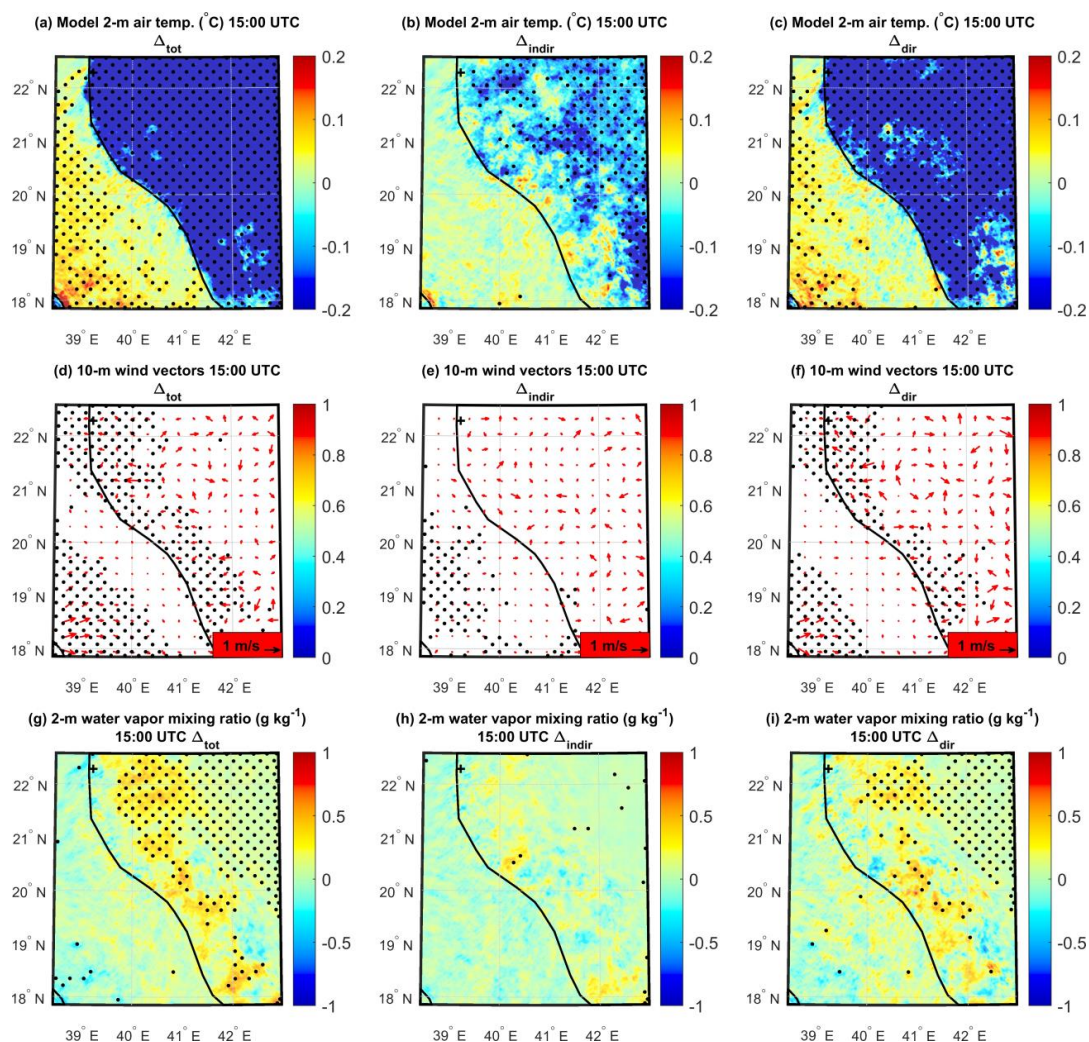
607 **3.3. Dust effect on rainfall**

608 **3.3.1. Dust direct and indirect effects**

609 Figure 13 (a, b, c) shows the dust effects on 2-m air temperature. Dust induces a total cooling
610 effect over the lands (Fig. 13a), which appear to be dominated by the direct effects (Fig. 13c)
611 rather than the indirect effects (Fig. 13b). Dust also induces warming in some inland areas and
612 over the ocean, which is affected by both the indirect and the direct effects (Figs. 13b and 13c).
613 The total and direct effects were largely statistically significant (black dots) but the indirect
614 effects were significant only over the lands.

615 In turn, the cooling and warming of the land surface affects the winds. Figures 13 (d, e, f) shows
616 the effects of dust on surface winds. As with surface temperature, the direct effects had a
617 stronger influence compared to the indirect effects on winds as well. The direct effects on winds
618 were statistically significant along the coast, which confirms the impact of dust's direct effects
619 on sea breezes.

620 A high positive moisture anomaly was observed over the land (Fig. 13 g, h, i), particularly with
621 the direct effect (Fig. 13i). The moisture increase over the land caused by the direct effect is
622 further amplified by the weaker indirect effect making the total effect more widespread. The
623 increased moisture due to the direct and total effect were both statistically significant. The reason
624 for the positive moisture anomaly over the land in relation to sea breeze is explained in the
625 section below.



626

627 Figure 13. Spatial patterns of the Δ_{tot} (F1-F2), Δ_{indir} (F3-F4), and Δ_{dir} $\{(F1-F2)-(F3-F4)\}$ for 2-m
 628 air temperature (a, b, c), 10-m winds (d, e, f) and 2-m water vapor mixing ratio (g, h, i) averaged
 629 at the time of rainfall maxima (15:00 UTC) over the entire study period (August 2006–2015).



630 Table 3. Total, indirect, and direct effects of dust on rainfall for extreme and normal rainfall
 631 events.

Case	Total effect (Δ_{tot})			Indirect effect (Δ_{indir})			Direct effect (Δ_{dir})		
	Domain average rainfall (mm) F1 all_aer	Domain average rainfall (mm) F2 no_dust	Effect (F1-F2) mm (%)*	Domain average rainfall (mm) F3 all_aer	Domain average rainfall (mm) F4 no_dust	Effect (F3-F4) mm (%)*	all_aer	no_dust	Effect (F1-F2) – (F3-F4) mm (%)*
Extreme rainfall events	2.404	2.264	0.140 (6.05)	2.347	2.242	0.105 (4.54)	0.057	0.022	0.035 (1.51)
	Significant? (p-value)		yes (0.004)	Significant? (p-value)		yes (0.048)	Significant? (p-value)		no (0.367)
Normal rainfall events	0.287	0.290	-0.003 (-1.02)	0.306	0.292	0.014 (4.76)	-0.019	-0.002	-0.017 (-5.78)
	Significant? (p-value)		no (0.083)	Significant? (p-value)		yes (<0.0001)	Significant? (p-value)		yes (<0.0001)

632 *Percentage of average rainfall (F1, F2, F3, and F4).

633 Table 3 summarizes the effects of dust on rainfall for extreme and normal rainfall events
 634 calculated in terms of a 10-year average daily-accumulated rainfall over the study domain (d03)
 635 during the month of August. For the extreme-rainfall events, the total effect (0.140 mm), indirect
 636 effect (0.105 mm), and direct effect (0.035 mm) were all positive (enhancement). The total,
 637 indirect, and direct effects in terms of percentage of average rainfall are 6.05, 4.54, and 1.51%,
 638 respectively. The total and indirect effects are significant at the assumed 5% significance level
 639 but not the direct effect. The direct effect, although small and statistically insignificant,
 640 contributed to the larger indirect effect making the total effect statistically significant.

641 For the normal-rainfall events, the change in rainfall amount due to total, indirect, and direct
 642 effects are -0.003, 0.014, and -0.017 mm, respectively. Both the rainfall changes from the
 643 indirect effect (positive) and the direct effect (negative) were statistically significant at the
 644 assumed 5% significance level. The total, indirect, and direct effects in terms of percentage of
 645 average rainfall were -1.02, 4.76, and -5.78%, respectively. The indirect and direct effects, which
 646 are opposite in sign and nearly equal in magnitude, cancel each other out making the total effect
 647 small but statistically insignificant. However, note that the total effect could be considered
 648 significant if the significance level was increased to 10% ($p = 0.083$).

649 Although the domain-average rainfall change caused by dust averaged over multiple years
 650 (2006–2015) appeared small, the effect can be large at different grid points and times. For
 651 example, for the year 2015, the accumulated rainfall changes (total effect) for August at the grid
 652 point maxima and minima within the domain were 92.0 mm (190.0%) and -70.0 mm (-46.6%),
 653 respectively.

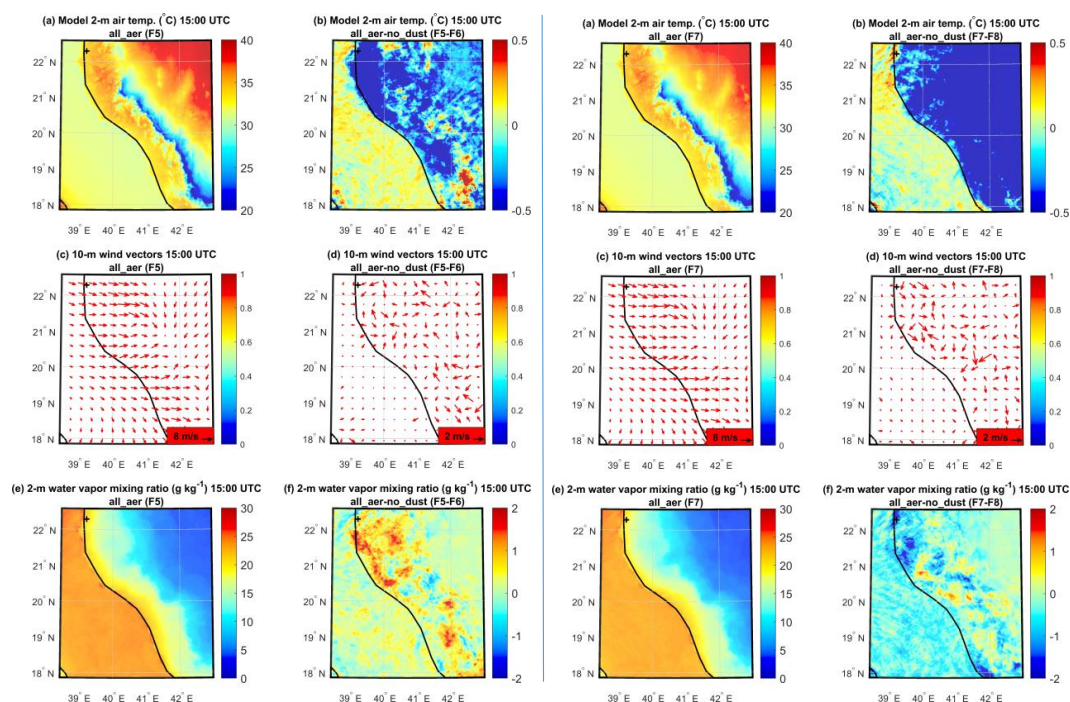
654 The total, indirect, and direct effects were also calculated for the total number of wet days
 655 (average daily-accumulated rainfall ≥ 1 mm). The number of wet days increased by three due to



656 the indirect effects but decreased by four by the direct effects, resulting in a total net increase of
657 one day.

658 Table 3 summarizes the dust direct effect (Δ_{dir}) calculated using the standard method mentioned
659 in section 2.3.2 [i.e., by subtracting the indirect effect (Δ_{indir}) from the total effect (Δ_{tot})]. To
660 verify the validity of this method, we compared the results obtained from this method with the
661 direct effect calculated from direct-effects-only experiments (F5, F6, Table 2) for Aug 2015. The
662 direct-effects-only experiments allow us to more directly calculate effects of dust on rainfall
663 induced by land surface cooling or warming using the same model but with simpler settings
664 without the indirect effects. The dust direct effect calculated from these direct-effects-only
665 simulations (-0.046 mm) agreed very well with the results obtained from the standard method (-
666 0.045 mm). The consistency of these two results confirms the robustness of our results.

667 3.3.2 Physical mechanism of the dust direct effects



668
669 Figure 14. Left two columns: spatial patterns of 2-m air temperature (a, b), 10-m wind vectors (c, d), and 2-m water vapor mixing ratio (e, f) averaged at the time of sea breeze maxima (15:00
670 UTC) throughout the period of August 4–31, 2015 from the direct-effects-only experiment for
671 all_aer case: F5 (first column) and the difference all_aer-no_dust: F5-F6 (second column). Right
672 two columns: same as the left panel but without shortwave absorption, showing all_aer case (F7)
673 and the difference all_aer-no_dust (F7-F8).
674

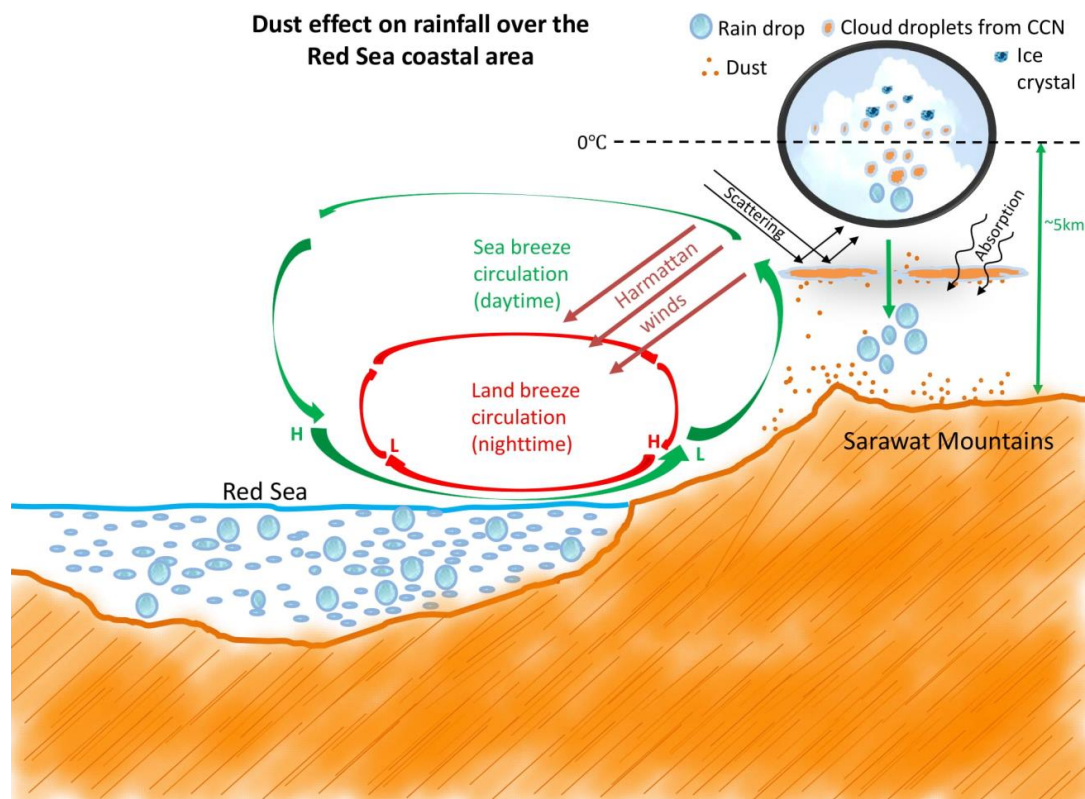


675 The results of the direct-effects-only simulations (F5, F6, Table 2) are presented in Fig. 14 (left
676 two columns). The cooling effect was dominant in the coastal areas, whereas warming was also
677 observed in some inland areas particularly in the southern region (Fig. 14b). Figure 14d
678 demonstrates that the breezes are weakening and even reversing from land to sea in the areas of
679 cooling ($\sim 22\text{N}$) due to the dust direct effects. However, in the areas that exhibited warming
680 ($\sim 18.5\text{N}$), sea breezes strengthened as the land warming further increased the land-sea thermal
681 contrast.

682 A strong positive moisture anomaly was observed over the land in the direct-effects-only
683 simulations (Fig. 14f, left two columns). This is intriguing because we expected a reduction in
684 moisture transport over the land due to the dust direct effects as a result of land surface cooling,
685 and a subsequent weakening of the sea breezes (Mostamandi et al., 2021). Figure 14 also shows
686 the results of the additional experiments in which the SW absorption was restricted (F7, F8), as
687 mentioned in section 2.3.2. Given that the SW absorption was eliminated, this experiment allows
688 us to better understand the effect of dust on sea breezes via the cooling effect alone (i.e., without
689 warming effects). However, note that the effect of dust is complex as it warms the atmosphere
690 and cools the surface (Choobari et al., 2014). Nevertheless, this elimination of SW absorption
691 removed the dust-induced warming observed earlier over the land (compare Figs. 14b left and
692 right panel). Since the cooling effect becomes dominant, sea breezes are now weaker and
693 therefore the landward moisture transport is considerably reduced, which is evident by
694 comparing the left and right panel of Figs. 15f. These results confirm that the high positive
695 moisture anomaly over the land by dust direct effects is caused by the strengthening of sea
696 breezes as a result of dust-induced warming. Although it is generally understood that SW
697 absorption decreases the radiation reaching the surface and thus cools the surface (e.g., Choobari
698 et al., 2014), we observed surface warming because most of the atmospheric dust here lie very
699 near to the surface (Parajuli et al., 2020), which is evident in Fig. 3b. The observed effects on
700 breezes are broadly consistent with those of Mostamandi et al. (2021), who also observed a
701 weakening of albedo-induced land cooling on sea breezes associated with the strong land
702 cooling, which reduces the thermal contrast between the land and the ocean.

703 **4. Summary discussion and limitations**

704 The rainfall over the Red Sea coastal area has a strong diurnal cycle peaking at approximately
705 15:00 UTC coinciding with the moisture-laden westerly sea breezes uplifted by the coastal
706 topography meeting the easterly Harmattan winds over the Sarawat Mountains. The dust
707 modifies rainfall through both indirect and direct effects over the study region by affecting the
708 sea breeze circulation. The various pathways of dust-rainfall interactions occurring over the Red
709 Sea coast are summarized in a schematic diagram presented in Fig. 15.



710

711 Figure 15. Schematic diagram representing the rainfall processes and dust-rainfall interactions
712 over the Red Sea coast.

713 In summary, dust enhances rainfall for extreme rainfall events but suppresses rainfall for normal
714 rainfall events. These results are consistent with previous studies (e.g., Choobari, 2018; Li et al.,
715 2011), which show that dust increases (decreases) rainfall in high (low) rainfall conditions. For
716 normal rainfall events, the suppressing direct effect is strong and significant, which is governed
717 by the weakening of the diurnal-scale sea breezes in response to SW cooling by dust. For
718 extreme rainfall events, the direct effect was positive but was not statistically significant, which
719 could perhaps become significant with a larger sample size. Physically, the direct effect in the
720 extreme rainfall events is governed by diverse synoptic processes and breezes do not play a
721 significant role in the effect.

722 Dust can modify cloud properties through both direct and indirect effects. The indirect effects are
723 positive because the dust directly contributes to the formation of CCN. This is evident in Fig.
724 S2b, which shows a statistically significant increase in cloud water mixing ratios over the lands
725 due to the indirect effects. As expected, the changes in clouds caused by the dust direct effects
726 are not statistically significant in most areas (Fig. S2c). Dust indirect effects are more complex
727 but aerosols are known to suppress rainfall at the initial stage of convection and enhances rainfall
728 during the mature stage through aerosol invigoration (Andreae et al., 2004; Koren et al., 2005;



729 Koren et al., 2008; Chakraborty et al., 2018; Fan et al., 2018). Increased aerosol concentration
730 can also increase cloud-top evaporation, thus reducing the cloud coverage (Choo Bari, 2018).

731 Dust evidently induces significant surface cooling and warming through indirect effects as well
732 (Fig. 13b), as clouds scatter and absorb shortwave radiation similar to dust. Therefore, we
733 concluded that the rain suppression (enhancement) over the study region is governed primarily
734 by dust-induced land surface cooling (warming) either directly or through clouds, which
735 ultimately decreases (increases) landward moisture transport by weakening (strengthening) sea
736 breeze circulation. It is also worth noting that the net effect of dust on surface temperature
737 through clouds depends on the cloud heights and other cloud properties.

738 In this study, we evaluated the relative contribution of direct and indirect effects of dust on
739 rainfall and explored associated physical mechanisms using well-developed microphysical and
740 aerosol schemes in WRF-Chem. Modeling rainfall processes entails some uncertainty, which is
741 mainly related to the effect of aerosols on clouds. There are several microphysical processes
742 governing dust-cloud-rainfall interactions that are not fully understood or implemented yet in
743 WRF-Chem (e.g., the prognostic treatment of ice nucleation by dust) (Chapman et al., 2009).
744 Therefore, our model simulations may have not captured some dust-cloud-rainfall interactions
745 occurring in reality, particularly those related to cold-cloud processes.

746 *Broader implications*

747 Through high-resolution model simulations, complemented with multiple observational data, we
748 investigated how dust affects rainfall over the Red Sea coastal region through direct and indirect
749 effects. Our study has broader social and environmental implications. While dust and dust storms
750 are generally considered detrimental from an air quality perspective, our study highlights their
751 contribution in modulating rain, an essential element of plant and animal life. A Better
752 understanding of regional rainfall process can be helpful for planning and managing regional
753 water resources as the replenishment of surface and ground water largely depends on
754 precipitation (Mostamandi et al., 2020). A better understanding of the dynamics of extreme
755 rainfall events could also aid in the development of strategies to minimize their catastrophic
756 outcomes such as heavy flooding and loss of public property (e.g., de Vries et al., 2013). Recent
757 studies suggest that there is an increase in the dust/aerosol activity in the region (e.g.,
758 Klingmüller et al., 2016). In this context, our model experiments (no_dust and all_aer) can also
759 provide insights into how increased dust activity affects regional rainfall patterns.

760 Our study also has implications from a cloud-seeding perspective, which is relevant in the
761 context of recent rainfall enhancement efforts over the region (e.g., Yanlong et al., 2017). Cloud
762 seeding experiments were conducted in the southwest of Saudi Arabia in the Asir mountainous
763 region in 2006–2008 using AgI, which receives a relatively high amount of precipitation
764 (Sinkevich and Krauss, 2010). Those results demonstrated the feasibility of cloud seeding over
765 the region by showing that the reflectivity of seeded clouds was significantly different compared
766 to that of natural clouds (Sinkevich and Krauss, 2010; Krauss et al., 2011). However, our results
767 suggest that cloud seeding efficiency may be affected by the presence of background dust
768 aerosols, and that it may not be as effective in dusty regions as in clean environments. Therefore,



769 before investing on expensive field experiments on cloud seeding, it would be beneficial to
770 evaluate the effectiveness of cloud seeding through regional modeling in the areas of interest as
771 done in this study.

772 5. Conclusion

773 Our study evaluated the effect of dust on rainfall over the Red Sea coastal plains using a double-
774 moment microphysics scheme (Morrison) combined with an advanced aerosol scheme
775 (MOSAIC) in WRF-Chem. The model captured the magnitude of AOD and aerosol vertical
776 profiles, the vertical profile of air temperature, the diurnal cycle of winds, spatio-temporal
777 variation of accumulated rainfall, and the CCN number concentrations over the study domain
778 reasonably well.

779 The rainfall over the Red Sea coast is mainly governed by warm cloud processes, which mainly
780 occur within a ~5 km height. Rainfall has a strong diurnal cycle, which peaks in the evening at
781 approximately 15:00 UTC (6 pm local time) under the influence of sea breezes.

782 We calculated the total, direct, and indirect effects of dust on rainfall for extreme and normal
783 rainfall events in terms of the 10-year (2006–2015) August average daily-accumulated rainfall
784 over the study domain (d_{03}). For extreme rainfall events (average daily-accumulated rainfall \geq
785 1.33 mm), dust causes a net enhancement on rainfall of 0.140 mm (6.05%), whereas the indirect
786 and the direct effects accounted for 0.105 mm (4.54 %) and 0.035 mm (1.51 %), respectively.
787 Although the positive direct effect is statistically insignificant at the assumed 5% significance
788 level, it adds up with the positive indirect effect, making the total effect significant. For the
789 normal rainfall events (average daily-accumulated rainfall $<$ 1.33 mm), dust causes a net
790 suppression of rainfall of -0.003 mm (-1.02 %), with the indirect and direct effects accounting for
791 0.014 (4.76 %), and -0.017 mm (-5.78 %), respectively, all of which were statistically significant.
792 The indirect and direct effects, which are opposite in sign and nearly equal in magnitude, cancel
793 each other out, making the total effect small but statistically significant.

794 Dust affects rainfall over the Red Sea coastal region through both direct and indirect effects by
795 influencing the sea breeze circulation. Dust induces land surface cooling caused by shortwave
796 scattering and warming caused mainly by shortwave absorption, which are further modulated by
797 its effect on clouds. Such land cooling (warming) ultimately weakens (strengthens) the sea
798 breeze circulation, thus reducing (increasing) the landward moisture transport and suppressing
799 (enhancing) coastal rainfall.

800 Given that the study area exhibit stable breeze circulation, our results could be extended to other
801 coastal areas with a topography that have similar breeze system. Importantly, our results have
802 broader scientific and environmental implications. Although dust is considered a nuisance from
803 an air quality perspective, our results highlight the more positive fundamental role of dust
804 particles in modulating rainfall formation and distribution. In the context of regional rain
805 enhancement efforts, our results also have implications for cloud seeding and regional water
806 resource management.



807 *Codes and data availability.* MODIS AOD data were downloaded from
808 <http://ladsweb.nascom.nasa.gov/data/>. MERRA-2 and IMERG data were obtained from the
809 NASA Goddard Earth Sciences Data and Information Services Center (GES DISC) available at
810 <https://disc.gsfc.nasa.gov/>. ECMWF Operational Analysis data are restricted data, which were
811 retrieved from [http://apps.ecmwf.int/archive-](http://apps.ecmwf.int/archive-catalogue/?type=4v&class=od&stream=oper&expver=1)
812 [catalogue/?type=4v&class=od&stream=oper&expver=1](http://apps.ecmwf.int/archive-catalogue/?type=4v&class=od&stream=oper&expver=1) with a membership. EDGAR-4.2 is
813 available at <http://edgar.jrc.ec.europa.eu/overview.php?v=42>. Field observation data and VIIRS
814 satellite data may be obtained by request to the first author at psagar@utexas.edu. A copy of the
815 namelist.input file with details of the WRF-Chem model configuration can be downloaded from
816 the KAUST repository at <http://hdl.handle.net/10754/675620>.

817 *Acknowledgements.* Our study was supported by funding from King Abdullah University of
818 Science and Technology (KAUST). We also thank Dr. Daniel Rosenfeld for his assistance in the
819 acquisition of VIIRS data. Battelle Memorial Institute operates PNNL under contract DEAC05-
820 76RL01830.

821 *Author contributions.* SPP and GLS developed the central scientific concept of the paper. SPP
822 analyzed the data and wrote the paper with inputs from GLS. SPP conducted the WRF-Chem
823 simulations, and AU contributed with code modifications. PK and DA processed and provided
824 data from the August 2009 field campaign in Saudi Arabia. YZ processed and provided the
825 VIIRS data. All authors discussed the results and contributed to the final manuscript.

826 *Competing interests.* The authors declare that they have no conflict of interest.

827



828 References

- 829 Abdul-Razzak, H., and Ghan, S. J., A parameterization of aerosol activation, 3, Sectional representation,
830 J. Geophys. Res., 107(D3), doi:10.1029/2001JD000483, 2002.
- 831 Andreae, M.O., Rosenfeld, D., Artaxo, P., Costa, A.A., Frank, G.P., Longo, K.M. and Silva-Dias, M.D.:
832 Smoking rain clouds over the Amazon, Science, 303(5662), 1337-1342,
833 <https://doi.org/10.1126/science.1092779>, 2004.
- 834 Abbott, T. H. and Cronin, T. W.: Aerosol invigoration of atmospheric convection through increases in
835 humidity, Science, 371 (6524), 83-85, <https://doi.org/10.1126/science.abc5181>, 2021.
- 836 Aina, Y.A., Van der Merwe, J. H. and Alshuwaikhat, H.M.: Spatial and Temporal Variations of Satellite-
837 Derived Multi-Year Particulate Data of Saudi Arabia: An Exploratory Analysis. International
838 Journal of Environmental Research and Public Health, 11, 11,152-11,166.
839 <https://doi.org/10.3390/ijerph11111152>, 2014.
- 840 Alam, M.M.: Impact of cloud microphysics and cumulus parameterization on simulation of heavy rainfall
841 event during 7–9 October 2007 over Bangladesh, Journal of earth system science, 123(2), 259-
842 279, <https://doi.org/10.1007/s12040-013-0401-0>, 2014.
- 843 Albrecht, B.A.: Aerosols, cloud microphysics, and fractional cloudiness, Science, 245(4923), 1227-1230,
844 <https://doi.org/10.1126/science.245.4923.1227>, 1989.
- 845 [Almazroui, M. and Saeed, S.: Contribution of extreme daily precipitation to total rainfall over the Arabian
846 Peninsula, Atmospheric Research, 231, 104672, https://doi.org/10.1016/j.atmosres.2019.104672,
847 2020.](https://doi.org/10.1016/j.atmosres.2019.104672)
- 848 Ansmann, A., Mattis, I., Müller, D., Wandinger, U., Radlach, M., Althausen, D., et al.: Ice formation in
849 Saharan dust over central Europe observed with temperature/humidity/aerosol Raman lidar,
850 Journal of Geophysical Research, 110, D18S12, <https://doi.org/10.1029/2004jd005000>, 2005.
- 851 Anisimov, A., Tao, W., Stenchikov, G., Kalenderski, S., Prakash, P. J., Yang, Z.-L., and Shi, M.:
852 Quantifying local-scale dust emission from the Arabian Red Sea coastal plain, Atmospheric
853 Chemistry and Physics, 17, 993–1015, <https://doi.org/10.5194/acp-17-993-2017>, 2017.
- 854 Bangalath, H. K., and Stenchikov, G. (2015), Role of dust direct radiative effect on the tropical rain belt
855 over Middle East and North Africa: A high-resolution AGCM study, J. Geophys. Res. Atmos.,
856 120, 4564– 4584. doi:10.1002/2015JD023122.
- 857 Bond, T. C., et al.: Bounding the role of black carbon in the climate system: A scientific assessment,
858 Journal of Geophysical Research, 118(11), 5380–5552, <https://doi.org/10.1002/jgrd.50171>, 2013.
- 859 Chakraborty, S., Fu, R., Rosenfeld, D., & Massie, S. T.: The influence of aerosols and meteorological
860 conditions on the total rain volume of the mesoscale convective systems over tropical continents,
861 Geophysical Research Letters, 45, 13,099– 13,106. <https://doi.org/10.1029/2018GL080371>, 2018.
- 862 Chapman, E. G., Gustafson Jr, W. I., Easter, R. C., Barnard, J. C., Ghan, S. J., Pekour, M. S., et al.:
863 Coupling aerosol-cloud-radiative processes in the WRF-Chem model: Investigating the radiative
864 impact of elevated point sources, Atmospheric Chemistry and Physics, 9(3), 945-964,
865 <https://doi.org/10.5194/acp-9-945-2009>, 2009.
- 866 Choobari, O.A., Zawar-Reza, P. and Sturman, A.: The global distribution of mineral dust and its impacts
867 on the climate system: A review, Atmospheric Research, 138, 152-165,
868 <https://doi.org/10.1016/j.atmosres.2013.11.007>, 2014.
- 869 Choobari, O., A.: Impact of aerosol number concentration on precipitation under different precipitation
870 rates. Meteorological Applications, 25, 596– 605, <https://doi.org/10.1002/met.1724>, 2018.
- 871 Choudhury, G., Tyagi, B., Vissa, N. K., Singh, J., Sarangi, C., Tripathi, S. N., and Tesche, M.: Aerosol-
872 enhanced high precipitation events near the Himalayan foothills, Atmospheric Chemistry and
873 Physics, 20, 15389–15399, <https://doi.org/10.5194/acp-20-15389-2020>, 2020.
- 874 Creamean, J. M., Suski, K. J., Rosenfeld, D., Cazorla, A., DeMott, P. J., Sullivan, R. C., et al.: Dust and
875 biological aerosols from the Sahara and Asia influence precipitation in the Western U.S, Science,
876 339(6127), 1572–1578, <https://doi.org/10.1126/science.1227279>, 2013.



- 877 Dagan, G., Koren, I., and Altaratz, O.: Competition between core and periphery-based processes in warm
878 convective clouds – from invigoration to suppression, *Atmospheric Chemistry and Physics*, *15*,
879 2749–2760, <https://doi.org/10.5194/acp-15-2749-2015>, 2015.
- 880 Deng, L., McCabe, M. F., Stenchikov, G., Evans, J. P., and P. A. Kucera, P. A.: Simulation of Flash-
881 Flood-Producing Storm Events in Saudi Arabia Using the Weather Research and Forecasting
882 Model, *Journal of Hydrometeorology*, *16*, 615–630, <https://doi.org/10.1175/JHM-D-14-0126.1>,
883 2015.
- 884 Dennis, A.S.: Weather modification by cloud seeding, *International geophysics series*, *24*, 670,
885 https://digitalcommons.usu.edu/water_rep/670, 1980.
- 886 Deshler, T., Reynolds, D. W. and Huggins, A. W.: Physical Response of Winter Orographic Clouds over
887 the Sierra Nevada to Airborne Seeding Using Dry Ice or Silver Iodide, *Journal of Applied*
888 *Meteorology*, *29*, 288–330, [https://doi.org/10.1175/1520-
889 0450\(1990\)029<0288:PROWOC>2.0.CO;2](https://doi.org/10.1175/1520-0450(1990)029<0288:PROWOC>2.0.CO;2), 1990.
- 890 de Vries, A. J., Tyrlis, E., Edry, D., Krichak, S. O., Steil, B., and Lelieveld, J.: Extreme precipitation
891 events in the Middle East: Dynamics of the Active Red Sea Trough, *Journal of Geophysical*
892 *Research*, *118*, 7087–7108, <https://doi.org/10.1002/jgrd.50569>, 2013.
- 893 Dubovik, O., Herman, M., Holdak, A., Lapyonok, T., Tanré, D., Deuzé, J. L., Ducos, F., Sinyuk, A., and
894 985 Lopatin, A.: Statistically optimized inversion algorithm for enhanced retrieval of aerosol 986
895 properties from spectral multi-angle polarimetric satellite observations, *Atmos. Meas. Tech.*, *4*,
896 987 975–1018, <https://doi.org/10.5194/amt-4-975-2011>, 2011.
- 897 Dye, J. E., & Baumgardner, D. (1984). Evaluation of the Forward Scattering Spectrometer Probe. Part I:
898 Electronic and Optical Studies, *Journal of Atmospheric and Oceanic Technology*, *1*(4), 329-344.
899 Retrieved Sep 14, 2021, from [https://journals.ametsoc.org/view/journals/atot/1/4/1520-
900 0426_1984_001_0329_eotfss_2_0_co_2.xml](https://journals.ametsoc.org/view/journals/atot/1/4/1520-0426_1984_001_0329_eotfss_2_0_co_2.xml).
- 901 Eck, T. F., et al.: Spatial and temporal variability of column-integrated aerosol optical properties in the
902 southern Arabian Gulf and United Arab Emirates in summer, *Journal of Geophysical Research*,
903 *113*, D01204, <https://doi.org/10.1029/2007JD008944>, 2008.
- 904 Fan, J., Rosenfeld, D., Zhang, Y., Giangrande, S.E., Li, Z., Machado, L.A., Martin, S.T., Yang, Y., Wang,
905 J., Artaxo, P. and Barbosa, H.M.: Substantial convection and precipitation enhancements by
906 ultrafine aerosol particles, *Science*, *359* (6374), 411-418,
907 <https://doi.org/10.1126/science.aan8461>, 2018.
- 908 Farrar, J., Lentz, S., Churchill, J., Bouchard, P., Smith, J., Kemp, J., Lord, J., Allsup, G., and Hosom, D.:
909 King Abdullah University of Science and Technology (KAUST) mooring deployment cruise and
910 fieldwork report, Technical report, Woods Hole Oceanographic Institution, WHOI-KAUST-
911 CTR-2009, *2*, 2009.
- 912 Fast, J. D., Gustafson, W. I., Easter, R. C., Zaveri, R. A., Barnard, J. C., Chapman, E. G., Grell, G. A.,
913 and Peckham, S. E.: Evolution of ozone, particulates, and aerosol direct radiative forcing in the
914 vicinity of Houston using a fully coupled meteorology-chemistry-aerosol model, *Journal of*
915 *Geophysical Research*, *111*, D21305, <https://doi.org/10.1029/2005JD006721>, 2006.
- 916 Forkel, R., Werhahn, J., Hansen, A. B., McKeen, S., Peckham, S., Grell, G., et al.: Effect of aerosol-
917 radiation feedback on regional air quality – A case study with WRF/Chem, *Atmospheric*
918 *Environment*, *53*, 202-211, <https://doi.org/10.1016/j.atmosenv.2011.10.009>, 2012.
- 919 Gao, W., Fan, J., Easter, R. C., Yang, Q., Zhao, C., and Ghan, S. J.: Coupling spectral-bin cloud
920 microphysics with the MOSAIC aerosol model in WRF-Chem: Methodology and results for
921 marine stratocumulus clouds, *Journal of Advances in Modeling Earth Systems*, *8*, 1289–1309,
922 <https://doi.org/10.1002/2016MS000676>, 2016.
- 923 Georgoulias, A.K., Marinou, E., Tsekeri, A., Proestakis, E., Akritidis, D., Alexandri, G., et al.: A First
924 Case Study of CCN Concentrations from Spaceborne Lidar Observations, *Remote*
925 *Sensing*, *12*(10), 1557, <https://doi.org/10.3390/rs12101557>, 2020.
- 926 Gibbons, J. D. and Chakraborti, S.: *Nonparametric Statistical Inference*, 5th Ed., Boca Raton, FL:
927 Chapman & Hall/CRC Press, Taylor & Francis Group, 2011.



- 928 Grabowski, W. W., and Morrison, H.: Do Ultrafine Cloud Condensation Nuclei Invigorate Deep
929 Convection?, *Journal of the Atmospheric Sciences*, 77(7), 2567-2583,
930 <https://doi.org/10.1175/JAS-D-20-0012.1>, 2020.
- 931 Grell, G.A., Peckham, S.E., Schmitz, R., McKeen, S.A., Frost, G., Skamarock, W.C. and Eder, B.: Fully
932 coupled “online” chemistry within the WRF model. *Atmospheric Environment*, 39(37), pp.6957-
933 6975, <https://doi.org/10.1016/j.atmosenv.2005.04.027>, 2005.
- 934 Gustafson, W. I., Chapman, E. G., Ghan, S. J., Easter, R. C., and Fast, J. D. (2007): Impact on modeled
935 cloud characteristics due to simplified treatment of uniform cloud condensation nuclei during
936 NEAQS 2004, *Geophysical Research Letters*, 34, L19809,
937 <https://doi.org/10.1029/2007GL030021>, 2007.
- 938 Han, Y., Fang, X., Zhao, T., Bai, H., Kang, S., and Song, L.: Suppression of precipitation by dust
939 particles originated in the Tibetan Plateau, *Atmospheric Environment*, 43(3), 568-574,
940 <https://doi.org/10.1016/j.atmosenv.2008.10.018>, 2009.
- 941 Hansen, J., Sato, M. and Ruedy, R.: Radiative forcing and climate response. *Journal of Geophysical*
942 *Research: Atmospheres*, 102(D6), 6831-6864, <https://doi.org/10.1029/96JD03436>, 1997.
- 943 Held, I. M., and Soden, B. J.: Robust Responses of the Hydrological Cycle to Global Warming, *Journal of*
944 *Climate*, 19(21), 5686-5699,
945 <https://journals.ametsoc.org/view/journals/clim/19/21/jcli3990.1.xml>, 2006.
- 946 Herich, H.; Tritscher, T.; Wiacek, A.; Gysel, M.; Weingartner, E.; Lohmann, U.; Baltensperger, U.;
947 Cziczo, D. J.: Water Uptake of Clay and Desert Dust Aerosol Particles at Sub- and Supersaturated
948 Water Vapor Conditions, *Physical Chemistry Chemical Physics*, 11, 7804– 7809,
949 <https://doi.org/10.1039/B901585J>, 2009.
- 950 Hollander, M. and Wolfe, D. A.: *Nonparametric Statistical Methods*, Hoboken, NJ: John Wiley & Sons,
951 Inc., 1999.
- 952 Hong, S.-Y., Yign N., and Dudhia, J.: A new vertical diffusion package with an explicit treatment of
953 entrainment processes, *Monthly Weather Review*, 134, 2318–2341,
954 <https://doi.org/10.1175/MWR3199.1>, 2006.
- 955 Huffman, G.J., E.F. Stocker, D.T. Bolvin, E.J. Nelkin, Jackson Tan (2019), *GPM IMERG Late*
956 *Precipitation L3 1 day 0.1 degree x 0.1 degree V06*, Edited by Andrey Savtchenko, Greenbelt,
957 MD, Goddard Earth Sciences Data and Information Services Center (GES DISC), Accessed: [Sep
958 12, 2021], [10.5067/GPM/IMERGDL/DAY/06](https://doi.org/10.5067/GPM/IMERGDL/DAY/06).
- 959 Iacono, M. J., Delamere, J. S., Mlawer, E. J., Shephard, M. W., Clough, S. A. and Collins, W. D.:
960 Radiative forcing by long-lived greenhouse gases: Calculations with the AER radiative transfer
961 models, *Journal of Geophysical Research*, 113, D13103, <https://doi.org/10.1029/2008JD009944>,
962 2008.
- 963 IPCC Climate Change 2013: The Physical Science Basis. Contribution of Working Group I to the Fifth
964 Assessment Report of the Intergovernmental Panel on Climate Change [Stocker, T.F., D. Qin, G.-
965 K. Plattner, M. Tignor, S.K. Allen, J. Boschung, A. Nauels, Y. Xia, V. Bex and P.M. Midgley
966 (eds.)], Cambridge University Press, Cambridge, United Kingdom and New York, NY, USA,
967 1535, <https://www.ipcc.ch/report/ar5/wg1/>, 2013.
- 968 Jacobson, M. Z. and Kaufman, Y. J.: Wind reduction by aerosol particles, *Geophysical Research*
969 *Letters*, 33, L24814, <https://doi.org/10.1029/2006GL027838>, 2006.
- 970 Jha, V., Cotton, W. R., Carrió, G. G., and Walko, R.: *Sensitivity Studies on the Impact of Dust and*
971 *Aerosol Pollution Acting as Cloud Nucleating Aerosol on Orographic Precipitation in the*
972 *Colorado River Basin, Advances in Meteorology*, 3041893,
973 <https://doi.org/10.1155/2018/3041893>, 2018.
- 974 Jha, V., Cotton, W. R., Carrió, G. G., Robert Walko, R. (2021) Seasonal estimates of the impacts of
975 aerosol and dust pollution on orographic precipitation in the Colorado River Basin, *Physical*
976 *Geography*, 42(1), 73-97, <https://doi.org/10.1080/02723646.2020.1792602>, 2021.



- 977 Jin, Q., Wei, J., Yang, Z.-L., Pu, B., and Huang, J.: Consistent response of Indian summer monsoon to
978 Middle East dust in observations and simulations, *Atmos. Chem. Phys.*, 15, 9897–9915,
979 <https://doi.org/10.5194/acp-15-9897-2015>, 2015.
- 980 Jones, C., Mahowald, N. and Luo, C.: Observational evidence of African desert dust intensification of
981 easterly waves, *Geophysical Research Letters*, 31, L17208, <https://doi.org/10.1029/2004GL020107>,
982 2004.
- 983 Joodaki, G., Wahr, J., and Swenson, S.: Estimating the human contribution to groundwater depletion in
984 the Middle East, from GRACE data, land surface models, and well observations, *Water*
985 *Resources Research*, 50, 2679–2692, <https://doi.org/10.1002/2013WR014633>, 2014.
- 986 Jordan, A. K., Zaitchik, B. F., Gnanadesikan, A., Kim, D., and Badr, H. S.: Strength of Linkages Between
987 Dust and Circulation Over North Africa: results from a coupled modeling system with active
988 dust, *Journal of Geophysical Research: Atmospheres*, 125, e2019JD030961,
989 <https://doi.org/10.1029/2019JD030961>, 2020.
- 990 [Kalenderski, S., and Stenchikov, G. \(2016\). High-resolution regional modeling of summertime transport
991 and impact of African dust over the Red Sea and Arabian Peninsula, *J. Geophys. Res. Atmos.*,
992 121, 6435–6458, doi:10.1002/2015JD024480.](#)
- 993 [Kawecki, S., & Steiner, A. L. \(2018\). The influence of aerosol hygroscopicity on precipitation intensity
994 during a mesoscale convective event. *Journal of Geophysical Research: Atmospheres*, 123, 424–
995 442. <https://doi.org/10.1002/2017JD026535>](#)
- 996 [Karydis, V. A., Kumar, P., Barahona, D., Sokolik, I. N., and Nenes, A. \(2011\). On the effect of dust
997 particles on global cloud condensation nuclei and cloud droplet number, *J. Geophys. Res.*, 116,
998 D23204, doi:10.1029/2011JD016283.](#)
- 999 [Keith, D. W., Weisenstein, D. K., Dykema, J. A. & Keutsch, F. N. Stratospheric solar geoengineering
1000 without ozone loss. *Proc. Natl Acad. Sci.* 113, 14910–14914 \(2016\).
1001 <https://doi.org/10.1073/pnas.1615572113>.](#)
- 1002 Khan, B., Stenchikov, G., Weinzierl, B., Kalenderski, S., and Osipov, S.: Dust plume formation in the
1003 free troposphere and aerosol size distribution during the Saharan Mineral Dust Experiment in
1004 North Africa, *Tellus B: Chemical and Physical Meteorology*, 67(1),
1005 <https://doi.org/10.3402/tellusb.v67.27170>, 2015.
- 1006 Konare, A., Zakey, A. S., Solmon, F., Giorgi, F., Rauscher, S., Ibrah, S., et al.: A regional climate
1007 modeling study of the effect of desert dust on the West African monsoon, *Journal of Geophysical*
1008 *Research*, 113, D12206, <https://doi.org/10.1029/2007JD009322>, 2008.
- 1009 Koehler, K. A., Kreidenweis, S. M., DeMott, P. J., Petters, M. D., Prenni, A. J., and Carrico, C. M.:
1010 Hygroscopicity and cloud droplet activation of mineral dust aerosol, *Geophysical Research*
1011 *Letters*, 36, L08805, <https://doi.org/10.1029/2009GL037348>, 2009.
- 1012 Klingmüller, K., Karydis, V. A., Bacer, S., Stenchikov, G. L., and Lelieveld, J.: Weaker cooling by
1013 aerosols due to dust–pollution interactions, *Atmospheric Chemistry and Physics*, 20, 15285–
1014 15295, <https://doi.org/10.5194/acp-20-15285-2020>, 2020.
- 1015 Klingmüller, K., Lelieveld, J., Karydis, V. A., and Stenchikov, G. L.: Direct radiative effect of dust–
1016 pollution interactions, *Atmos. Chem. Phys.*, 19, 7397–7408, [https://doi.org/10.5194/acp-19-7397-
1017 2019](https://doi.org/10.5194/acp-19-7397-2019), 2019.
- 1018 Klingmüller, K., Pozzer, A., Metzger, S., Stenchikov, G. L., and Lelieveld, J.: Aerosol optical depth trend
1019 over the Middle East, *Atmospheric Chemistry and Physics*, 16, 5063–5073,
1020 <https://doi.org/10.5194/acp-16-5063-2016>, 2016.
- 1021 Kondapalli, N. K. and Suzuki, K.: Assessment of seasonal cloud properties in the United Arab Emirates
1022 and adjoining regions from geostationary satellite data, *Remote Sensing of Environment*, 228, 90–
1023 104, <https://doi.org/10.1016/j.rse.2019.04.024>, 2019.
- 1024 Koren, I., Kaufman, Y. J., Rosenfeld, D., Remer, L. A., and Rudich, Y.: Aerosol invigoration and
1025 restructuring of Atlantic convective clouds, *Geophysical Research Letters*, 32, L14828,
1026 <https://doi.org/10.1029/2005GL023187>, 2005.



- 1027 Koren, I., Martins, J.V., Remer, L.A. and Afargan, H.: Smoke invigoration versus inhibition of clouds
1028 over the Amazon, *Science*, 321(5891), 946-949, <https://doi.org/10.1126/science.1159185>, 2008.
- 1029 Koren, I., Dagan, G. and Altaratz, O.: From aerosol-limited to invigoration of warm convective clouds,
1030 *Science*, 344(6188), 1143-1146, <https://doi.org/10.1126/science.1252595>, 2014.
- 1031 Krauss, T.W., Sinkevich, A.A. and Ghulam, A.S.: Effects of feeder cloud merging on storm development
1032 in Saudi Arabia, *Journal of King Abdulaziz University: Metrology, Environment and Arid Land*
1033 *Agricultural Sciences*, 142(592), 1-33, <https://doi.org/10.4197/Met.22-2.2.2011>.
- 1034 Kucera, P., Axisa, D., Burger, R.P., Collins, D.R., Li, R., Chapman, M., et al.: Features of the Weather
1035 Modification Assessment Project in Southwest Region of Saudi Arabia, *The Journal of Weather*
1036 *Modification*, 42(1), 78-103, 2010.
- 1037 Lau, W. K. M., Kim, M.-K., Kim, K.-M. and Lee, W.-S.: Enhanced surface warming and accelerated
1038 snow melt in the Himalayas and Tibetan Plateau induced by absorbing aerosols, *Environmental*
1039 *Research Letters*, 5, 025204, <https://doi.org/10.1088/1748-9326/5/2/025204>, 2010.
- 1040 Lee, S.S.: Effect of Aerosol on Circulations and Precipitation in Deep Convective Clouds, *Journal of*
1041 *Atmospheric Science*, 69, 1957–1974, <https://doi.org/10.1175/JAS-D-11-0111.1>, 2012, 2012.
- 1042 Li, R., Min, Q. and Harrison, L. C.: A Case Study: The Indirect Aerosol Effects of Mineral Dust on Warm
1043 Clouds, *Journal of Atmospheric Science*, 67, 805–816, <https://doi.org/10.1175/2009JAS3235.1>,
1044 2010.
- 1045 Li, Z., Niu, F., Fan, J., Liu, Y., Rosenfeld, D. and Ding, Y.: Long-term impacts of aerosols on the vertical
1046 development of clouds and precipitation, *Nature Geoscience*, 4(12), 888-894,
1047 <https://doi.org/10.1038/ngeo1313>, 2011.
- 1048 Lim, K. S., and Hong, S.: Development of an Effective Double-Moment Cloud Microphysics Scheme
1049 with Prognostic Cloud Condensation Nuclei (CCN) for Weather and Climate Models, *Monthly*
1050 *Weather Review*, 138, 1587-1612, <https://doi.org/10.1175/2009MWR2968.1>, 2010.
- 1051 Liu, Z., Ostrenga, D., Teng, W. and Kempler, S.: Tropical Rainfall Measuring Mission (IMERG)
1052 Precipitation Data and Services for Research and Applications, *Bulletin of American*
1053 *Meteorological Society*, 93, 1317–1325, <https://doi.org/10.1175/BAMS-D-11-00152.1>, 2012.
- 1054 Lohmann, U. and Feichter, J.: Can the direct and semi-direct aerosol effect compete with the indirect
1055 effect on a global scale?, *Geophysical Research Letters*, 28(1), 159-161,
1056 <https://doi.org/10.1029/2000GL012051>, 2001.
- 1057 Lopatin, A., Dubovik, O., Fuertes, D., Stenchikov, G., Lapyonok, T., Veselovskii, I., Wienhold, F. G.,
1058 Shevchenko, I., Hu, Q., and Parajuli, S.: Synergy processing of diverse ground-based remote
1059 sensing and in situ data using GRASP algorithm: applications to radiometer, lidar and radiosonde
1060 observations, *Atmos. Meas. Tech. Discuss.* [preprint], [https://doi.org/10.5194/amt-2020-422_in](https://doi.org/10.5194/amt-2020-422_in_review)
1061 [review](https://doi.org/10.5194/amt-2020-422_in_review), 2020.
- 1062 Marengo, F., Ryder, C., Estellés, V., O'Sullivan, D., Brooke, J., Orgill, L., Lloyd, G., and Gallagher, M.:
1063 Unexpected vertical structure of the Saharan Air Layer and giant dust particles during AER-D,
1064 *Atmos. Chem. Phys.*, 18, 17655–17668, <https://doi.org/10.5194/acp-18-17655-2018>, 2018.
- 1065 Michibata, T., and Takemura, T.: Evaluation of autoconversion schemes in a single model framework
1066 with satellite observations, *Journal of Geophysical Research Atmospheres*, 120, 9570– 9590,
1067 <https://doi.org/10.1002/2015JD023818>, 2015.
- 1068 Miller, S. T. K., Keim, B. D., Talbot, R. W., and Mao, H.: Sea breeze: Structure, forecasting, and impacts,
1069 *Reviews of Geophysics*, 41, 1011, <https://doi.org/10.1029/2003RG000124>, 2003.
- 1070 Morrison, H., Thompson, G. and Tatarskii, V.: Impact of Cloud Microphysics on the Development of
1071 Trailing Stratiform Precipitation in a Simulated Squall Line: Comparison of One- and Two-
1072 Moment Schemes, *Monthly Weather Review*, 137, 991–
1073 1007, <https://doi.org/10.1175/2008MWR2556.1>, 2009.
- 1074 Min, Q.-L., Li, R., Lin, B., Joseph, E., Wang, S. and Hu, Y. et al.: Evidence of mineral dust altering cloud
1075 microphysics and precipitation, *Atmospheric Chemistry and Physics*, 9, 3223–3231,
1076 <https://doi.org/10.5194/acp-9-3223-2009>, 2009.



- 1077 Mlawer, E. J., Taubman, S. J., Brown, P. D., Iacono, M. J., and Clough, S. A.: Radiative transfer for
1078 inhomogeneous atmospheres: RRTM, a validated correlated-k model for the longwave, *Journal of*
1079 *Geophysical Research*, 102(D14), 16663– 16682. <https://doi.org/10.1029/97JD00237>, 1997.
- 1080 Muhs, D. R.: The geologic records of dust in the Quaternary, *Aeolian Research*, 9, 3-48,
1081 <https://doi.org/10.1016/j.aeolia.2012.08.001>, 2013.
- 1082 [Nazzari, Y., Barbulescu, A., Howari, F. et al.: New insights on sand dust storm from historical records,](#)
1083 [UAE, *Arabian Journal of Geosciences*, 12, 396, <https://doi.org/10.1007/s12517-019-4555-1>,](#)
1084 [2019.](#)
- 1085 Parajuli, S. P and Zender, C.: Connecting geomorphology to dust emission through high-resolution
1086 mapping of global land cover and sediment supply, *Aeolian Research*, 27, 47-65,
1087 doi:10.1016/j.aeolia.2017.06.002, 2017.
- 1088 Parajuli, S. P., Stenchikov, G. L., Ukhov, A., & Kim, H.: Dust emission modeling using a new high-
1089 resolution dust source function in WRF-Chem with implications for air quality, *Journal of*
1090 *Geophysical Research: Atmospheres*, 124, 10109–10133, <https://doi.org/10.1029/2019JD030248>,
1091 2019.
- 1092 Parajuli, S. P., Stenchikov, G. L., Ukhov, A., Shevchenko, I., Dubovik, O., and Lopatin, A.: Aerosol
1093 vertical distribution and interactions with land/sea breezes over the eastern coast of the Red Sea
1094 from lidar data and high-resolution WRF-Chem simulations, *Atmos. Chem. Phys.*, 20, 16089–
1095 16116, <https://doi.org/10.5194/acp-20-16089-2020>, 2020.
- 1096 Pu, B. and Ginoux, P.: Projection of American dustiness in the late 21st century due to climate change,
1097 *Scientific Reports*, 7, 5553, <https://doi.org/10.1038/s41598-017-05431-9>, 2017,
- 1098 Rémy, S., Benedetti, A., Bozzo, A., Haiden, T., Jones, L., Razinger, M., et al.: Feedbacks of dust and
1099 boundary layer meteorology during a dust storm in the eastern Mediterranean, *Atmospheric*
1100 *Chemistry and Physics*, 15, 12909–12933, <https://doi.org/10.5194/acp-15-12909-2015>, 2015.
- 1101 [Rienecker, M. M., et al.: MERRA: NASA's modern-era retrospective analysis for research and](#)
1102 [applications, *Journal of Climate*, 24\(14\), 3624–3648, <https://doi.org/10.1175/JCLI-D-11-00015.1>,](#)
1103 [2011.](#)
- 1104 [G. C. Roberts & A. Nenes \(2005\) A Continuous-Flow Streamwise Thermal-Gradient CCN Chamber for](#)
1105 [Atmospheric Measurements, *Aerosol Science and Technology*, 39:3, 206-](#)
1106 [221, DOI: 10.1080/027868290913988.](#)
- 1107 Robock, A., Bunzl, M., Kravitz, B. and Stenchikov, G.L.: A test for geoengineering?, *Science*, 327(5965),
1108 530-531, <https://doi.org/10.1126/science.1186237>, 2010.
- 1109 Rosenfeld, D., Rudich, Y. Ronen Lahav, R.: Desert dust suppression precipitation: A possible
1110 desertification feedback loop, *Proceedings of the National Academy of Sciences*, 98(11), 5975-
1111 5980; <https://doi.org/10.1073/pnas.101122798>, 2001.
- 1112 Schulzweida, U., Kornbluh, L. and Quast, R.: CDO user's guide, *Climate data operators*, version 1(6),
1113 2006.
- 1114 Shawon, A. S. M., Prabhakaran, P., Kinney, G., Shaw, R. A., and Cantrell, W.: Dependence of aerosol-
1115 droplet partitioning on turbulence in a laboratory cloud, *Journal of Geophysical Research:*
1116 *Atmospheres*, 126, e2020JD033799, <https://doi.org/10.1029/2020JD033799>, 2021.
- 1117 Sinkevich, A.A. and Krauss, T.W.: Cloud modification in Saudi Arabia: Statistical estimation of the
1118 results, *Russian Meteorology and Hydrology*, 35, 378–385,
1119 <https://doi.org/10.3103/S1068373910060038>, 2010.
- 1120 Simpson, J. E.: Sea breeze and local winds, Cambridge University Press, 1994.
- 1121 Solmon, F., Mallet, M., Elguindi, N., Giorgi, F., Zakey, A., and Konaré, A.: Dust aerosol impact on
1122 regional precipitation over western Africa, mechanisms and sensitivity to absorption properties,
1123 *Geophysical Research Letters*, 35, L24705, <https://doi.org/10.1029/2008GL035900>, 2008.
- 1124 Solomos, S., Kallos, G., Kushta, J., Astitha, M., Tremback, C., Nenes, A.: An integrated modeling study
1125 on the effects of mineral dust and sea salt particles on clouds and precipitation, *Atmospheric*
1126 *Chemistry and Physics*, 11, 873–892, <https://doi.org/10.5194/acp-11-873-2011>, 2011.



- 1127 Spurny, K. R.: Atmospheric Condensation Nuclei P. J. Coulier 1875 and J. Aitken 1880 (Historical
1128 Review), *Aerosol Science and Technology*, 32:3, 243-248,
1129 <https://doi.org/10.1080/027868200303777>, 2000.
- 1130 Stenchikov, G. L., Kirchner, I., Robock, A., Graf, H.-F., Antuña, J. C., Grainger, R. G., Lambert, A., and
1131 Thomason, L.: Radiative forcing from the 1991 Mount Pinatubo volcanic eruption. *Journal of*
1132 *Geophysical Research*, 103(D12), 13837– 13857. <https://doi.org/10.1029/98JD00693>, 1998.
- 1133 Stull, R. (2000). *Meteorology for scientists and engineers*. Brooks/Cole, 2000.
- 1134 Tang, M., Cziczo, D. J. and Grassian, V. H.: Interactions of Water with Mineral Dust Aerosol: Water
1135 Adsorption, Hygroscopicity, Cloud Condensation, and Ice Nucleation, *Chemical Reviews*, 116
1136 (7), 4205-4259, <https://doi.org/10.1021/acs.chemrev.5b00529>, 2016.
- 1137 Tewari, M., Chen, F., Wang, W., Dudhia, J., LeMone, M., Mitchell, K., Ek, M., Gayno, G., Wegiel, J.
1138 and Cuenca, R. H.: Implementation and verification of the unified NOAA land surface model in
1139 the WRF model, 20th conference on weather analysis and forecasting/16th conference on
1140 numerical weather prediction, 11–15, 2004.
- 1141 Trinh, T.-A., Feeny, S. and Posso, A.: Rainfall shocks and child health: the role of parental mental health,
1142 *Climate and Development*, <https://doi.org/10.1080/17565529.2020.1716672>, 2020.
- 1143 Tsvieli, Y. and Zangvil, A.: Synoptic climatological analysis of ‘wet’ and ‘dry’ Red Sea troughs over
1144 Israel, *International Journal of Climatology*, 25(15), 1997–2015, <https://doi.org/10.1002/joc.123>,
1145 2005.
- 1146 Tuccella, P., Curci, G., Grell, G. A., Visconti, G., Crumeyrolle, S., Schwarzenboeck, A., and Mensah, A.
1147 A.: A new chemistry option in WRF-Chem v. 3.4 for the simulation of direct and indirect aerosol
1148 effects using VBS: evaluation against IMPACT-EUCAARI data, *Geosci. Model Dev.*, 8, 2749–
1149 2776, <https://doi.org/10.5194/gmd-8-2749-2015>, 2015.
- 1150 Twohy, C.H.: Measurements of Saharan Dust in Convective Clouds over the Tropical Eastern Atlantic
1151 Ocean., *Journal of Atmospheric Science*, 72, 75–81, <https://doi.org/10.1175/JAS-D-14-0133.1>,
1152 2015.
- 1153 Twomey, S. A.: Aerosols, clouds and radiation, *Atmospheric Environment, Part A*, 25, 2435-2442,
1154 [https://doi.org/10.1016/0960-1686\(91\)90159-5](https://doi.org/10.1016/0960-1686(91)90159-5), 1991.
- 1155 Ukhov, A., Mostamandi, S., da Silva, A., Flemming, J., Alshehri, Y., Shevchenko, I., and Stenchikov, G.:
1156 Assessment of natural and anthropogenic aerosol air pollution in the Middle East using MERRA-
1157 2, CAMS data assimilation products, and high-resolution WRF-Chem model simulations,
1158 *Atmospheric Chemistry and Physics*, 20, 9281–9310, <https://doi.org/10.5194/acp-20-9281-2020>,
1159 2020.
- 1160 Ukhov, A., Ahmadov, R., Grell, G., and Stenchikov, G.: Improving dust simulations in WRF-Chem
1161 v4.1.3 coupled with the GOCART aerosol module, *Geosci. Model Dev.*, 14, 473–493,
1162 <https://doi.org/10.5194/gmd-14-473-2021>, 2021.
- 1163 Yamashita, K., Murakami, M., Hashimoto, A., Tajiri, T.: CCN Ability of Asian Mineral Dust Particles
1164 and Their Effects on Cloud Droplet Formation, *Journal of Meteorological Society of Japan*, 89,
1165 581–587, 2011.
- 1166 Yang, Q., W. I. Gustafson Jr., Fast, J. D., Wang, H., Easter, R. C., Morrison, H., Lee, Y.-N., Chapman, E.
1167 G., Spak, S. N., and Mena-Carrasco, M. A.: Assessing regional scale predictions of aerosols,
1168 marine stratocumulus, and their interactions during VOCALS-REx using WRF-Chem,
1169 *Atmospheric Chemistry and Physics*, 11, 11951–11975, [https://doi.org/10.5194/acp-11-11951-](https://doi.org/10.5194/acp-11-11951-2011)
1170 [2011](https://doi.org/10.5194/acp-11-11951-2011), 2011.
- 1171 Yang, Q., Gustafson Jr., W. I., Fast, J. D., Wang, H., Easter, R. C., Wang, M., Ghan, S. J., Berg, L. K.,
1172 Leung, L. R., and Morrison, H.: Impact of natural and anthropogenic aerosols on stratocumulus
1173 and precipitation in the Southeast Pacific: a regional modelling study using WRF-Chem,
1174 *Atmospheric Chemistry and Physics*, 12, 8777–8796, <https://doi.org/10.5194/acp-12-8777-2012>,
1175 [2012](https://doi.org/10.5194/acp-12-8777-2012).



- 1176 Yanlong Tai, Haoran Liang, Abdelali Zaki, Nabil El Hadri, Ali M. Abshaev, Buzgigit M. Huchunaev,
1177 Steve Griffiths, Mustapha Jouiad, and Linda Zou, ACS Nano, 11(12), 12318–12325,
1178 <https://doi.org/10.1021/acsnano.7b06114>, 2017.
- 1179 Yin, Y. and Chen, L.: The effects of heating by transported dust layers on cloud and precipitation: a
1180 numerical study, Atmospheric Chemistry and Physics, 7, 3497–3505. [https://doi.org/10.5194/acp-](https://doi.org/10.5194/acp-7-3497-2007)
1181 [7-3497-2007](https://doi.org/10.5194/acp-7-3497-2007), 2007.
- 1182 Yin, Y., Wurzler, S., Levin, Z., and Reisin, T. G.: Interactions of mineral dust particles and clouds:
1183 Effects on precipitation and cloud optical properties, Journal of Geophysical Research, 107(D23),
1184 4724, doi:[10.1029/2001JD001544](https://doi.org/10.1029/2001JD001544), 2002.
- 1185 Zaveri, R. A. and Peters, L. K.: A new lumped structure photochemical mechanism for large-scale
1186 applications, Journal of geophysical Research, 104, 30387–30415.
1187 <https://doi.org/10.1029/1999JD900876>, 1999.
- 1188 Zaveri, R. A., Easter, R. C., Fast, J. D., and Peters, L. K.: Model for Simulating Aerosol Interactions and
1189 Chemistry (MOSAIC), Journal of geophysical Research, 113, D13204,
1190 [https://10.1029/2007JD008782](https://doi.org/10.1029/2007JD008782), 2008.
- 1191 Zeinab S., Z., Steiner, A., Zakey, A. S., Shalaby, A. and Wahab, M. M. A.: An exploration of the aerosol
1192 indirect effects in East Asia using a regional climate model, *Atmósfera*, 33(1), 87–103,
1193 <https://doi.org/10.20937/ATM.52604>, 2020.
- 1194 Zhang, Y., Wang, K. and He, J.: Multi-year application of WRF-CAM5 over East Asia-Part II:
1195 Interannual variability, trend analysis, and aerosol indirect effects, Atmospheric Environment,
1196 165, 222–239, <https://doi.org/10.1016/j.atmosenv.2017.06.029>, 2017.
- 1197 Zhang, Y., He, J., Zhu, S., and Gantt, B.: Sensitivity of simulated chemical concentrations and aerosol-
1198 meteorology interactions to aerosol treatments and biogenic organic emissions in WRF/Chem,
1199 Journal of Geophysical Research: Atmosphere, 121, 6014–6048,
1200 <https://doi.org/10.1002/2016JD024882>, 2016.
- 1201 Zhao, B., Wang, Y., Gu, Y., Liou, K. –N., Jiang, J. H., Fan, J. et al.: Ice nucleation by aerosols from
1202 anthropogenic pollution, *Nature Geoscience*, 12, 602–607, [https://doi.org/10.1038/s41561-019-](https://doi.org/10.1038/s41561-019-0389-4)
1203 [0389-4](https://doi.org/10.1038/s41561-019-0389-4), 2019.
- 1204 Zhao, C., Liu, X., Ruby Leung, L., and Hagos, S. (2011). Radiative impact of mineral dust on monsoon
1205 precipitation variability over West Africa. *Atmospheric Chemistry and Physics*, 11, 1879–1893.
1206 <https://doi.org/10.5194/acp-11-1879-2011>, 2011.
- 1207 Zhao, C., Liu, X., Leung, L. R., Johnson, B., McFarlane, S. A., Gustafson Jr., W. I. et al.: The spatial
1208 distribution of mineral dust and its shortwave radiative forcing over North Africa: modeling
1209 sensitivities to dust emissions and aerosol size treatments, Atmospheric Chemistry and Physics,
1210 10, 8821–8838, <https://doi.org/10.5194/acp-10-8821-2010>, 2010.